Numerical Simulation of a Cross Flow Marine Hydrokinetic Turbine.

Taylor Jessica Hall

A thesis submitted in partial fulfillment
of the requirements for the degree of

Master of Science in Mechanical Engineering

University of Washington

2012

Program Authorized to Offer Degree: Mechanical Engineering

University of Washington

Abstract

Numerical Simulation of a Cross Flow Marine Hydrokinetic Turbine.

Taylor Jessica Hall

:

In the search for clean, renewable energy, the kinetic energy of water currents in oceans, rivers, and estuaries is being studied as a predictable and environmentally benign source. We investigate the flow past a cross flow hydrokinetic turbine (CFHT) in which a helical blade turns around a shaft perpendicular to the free stream under the hydrodynamic forces exerted by the flow. This type of turbine, while very different from the classical horizontal axis turbine commonly used in the wind energy field, presents advantages in the context of hydrokinetic energy harvesting, such as independence from current direction, including reversibility, stacking, and self-starting without complex pitch mechanisms. This thesis develops a numerical simulation methodology that applies the Reynolds Average Navier Stokes equations and the three-dimensional sliding mesh technique to model CFHTs. The methodology is validated against small scale experiments, available within NNMREC at the University of Washington and is used to investigate the efficiency of the energy capture and the hydrodynamic forces acting on the blades. First, we study the stationary turbine and conclude that the developed methodology accurately models the starting torque of a turbine initially in static conditions; some limitations are found, however, in predicting separated flow. The dynamic performance of the rotating turbine is predicted with reasonable accuracy using the sliding mesh technique. Excellent qualitative agreement with experimental trends is found in the results, and the ac-

tual predicted values from the simulations show good agreement with measurements. Though limitations in accurately modeling dynamic stall for the rotating turbine are confirmed, the good qualitative agreement suggests this methodology can be used to support turbine design and performance over a wide range of parameters, minimizing the number of prototypes to build and experiments to run in the pursuit of an optimized turbine. This methodology can also provide a cost-effective way of evaluating detailed full scale effects, such as mooring lines or local bottom bathymetry features, on both turbine performance and environmental assessment.

TABLE OF CONTENTS

Page

List of Figures iii

List of Tables v

Chapter 1: Introduction 1
- 1.1 Renewable Energy 1
- 1.2 Tidal Energy 2
- 1.3 Turbines 4
- 1.4 Hydrodynamics of Cross Flow Turbines 10

Chapter 2: Background 17
- 2.1 Motivation and Goals 17
- 2.2 Turbine Parameters 18
- 2.3 Literature Review 20

Chapter 3: Methodology 34
- 3.1 Renolds Average Navier Stokes Equations 34
- 3.2 Turbulence Closure Models 35
- 3.3 Near Wall Modeling 36
- 3.4 Sliding Mesh Model 39
- 3.5 Computational Domain and Boundary Conditions 41
- 3.6 Space Discretization 43
- 3.7 Evaluation Parameters 47

Chapter 4: Static Torque Analysis 50
- 4.1 Experiment Setup 50
- 4.2 Single Blade Simulations 51

4.3 Four Blade Simulations 54

Chapter 5: Rotating Turbine: Dynamic Torque Analysis 59
5.1 Single-Bladed Rotating Turbine 59
5.2 Four-Bladed Rotating Turbine 76

Chapter 6: Summary, Conclusions and Future Work 83
6.1 Numerical Methodology 84
6.2 Analysis of the Static Turbine Performance: Starting Torque 84
6.3 Summary of Dynamic Turbine Analysis 86
6.4 Conclusions and Future Work 89

LIST OF FIGURES

Figure Number — Page

1.1 Schematic of Spring and Neap tides formation based on the sun, moon, and earth orientation . . . 3
1.2 Schematic of axial flow vs. cross flow turbines . . . 5
1.3 Various tidal turbine designs from leading commercial companies . . . 6
1.4 Schematics of potential cross flow water turbine array designs . . . 8
1.5 CFWT examples for Darrieus, Gorlov, and Achard turbines . . . 9
1.6 Schematic of azimuthal position and velocity triangle for a cross flow water turbine . . . 11
1.7 Schematic of angle of attack, lift, and drag . . . 13
1.8 Plot of angle of attack vs. azimuthal position for various tip speed ratios 13
1.9 Plot of relative Reynolds number vs. azimuthal position for various tip speed ratios . . . 15

2.1 Schematics of variations of streamtube momentum models . . . 22
2.2 Schematic of Vortex model blade representation . . . 23
2.3 Schematic of Cascade model . . . 25
2.4 Flow fields demonstrating straightening effect from a tidal turbine barrage . . . 28

3.1 Three divisions of near wall region. . . . 38
3.2 Schematic of wall function and near wall modeling approach. . . . 39
3.3 Representation of stationary and rotating domains in the channel . . . 40
3.4 Schematic of non-conformal boundary interface . . . 41
3.5 Top and side views of channel domain with boundary conditions . . . 42
3.6 Visual representation of blockage ratio . . . 43
3.7 Mesh in xy plane for a single static blade . . . 44
3.8 Oval mesh for modeling a single static blade . . . 45
3.9 C-mesh for modeling in the near wall region . . . 46

3.10 Full turbine configuration with end plates and central shaft 47
3.11 Sliding mesh interface 48

4.1 Coefficient of torque for a single static blade 52
4.2 Velocity contour plots of static blade for various angle of attacks . . 54
4.3 Coefficient of torque for a single static blade including near-wall modeling 55
4.4 Coefficient of torque for a static four-bladed turbine 56
4.5 Coefficient of static torque for experiments 57
4.6 Coefficient of torque for CFD: single-bladed and four-bladed turbines 58

5.1 Plot of dynamic torque results for mesh-grids of different refinement levels for $\lambda = 3.2$ 60
5.2 Numerical Simulations for a single rotating blade 62
5.3 Free body diagram of dynamic torque system 65
5.4 Angular velocity in the single rotating blade experiment 66
5.5 Angular acceleration in the single rotating blade experiment 66
5.6 Torque in the single rotating blade experiment 68
5.7 Torque for a single rotating blade 70
5.8 Theoretical Reynolds number and angle of attack for the tip speed ratios occurring for $\lambda_{avg} = 3.2$ and $\lambda_{avg} = 3.8$ 71
5.9 Drag and lift data for a NACA 0018 airfoil from Sandia National Laboratory experiments 72
5.10 Difference between CFD and experiment instantaneous torque 73
5.11 Instantaneous and average torque for a single blade rotating at $\lambda = 3.2$ 76
5.12 Instantaneous and average torque for four-bladed turbine rotating at $\lambda = 1.6$ 77
5.13 Instantaneous torque for a single-bladed turbine and four-bladed turbine rotating at $\lambda = 1.6$ 78
5.14 CFD predicted torque values vs. tip speed ratio 79
5.15 Torque and power curves for a four bladed turbine 80

LIST OF TABLES

Table Number Page

2.1 Blade and Turbine Parameters 18
2.2 Calculated Turbine Parameters 20
3.1 Fluent Settings and Solution Methods 49
5.1 Mesh-Grids for a Single Rotating Blade 60
5.2 Simulation Torque Averages for the Single Rotating Blade 61
5.3 Average Coefficient of Torque for Single Rotating Blade 73

ACKNOWLEDGMENTS

I am sincerely ever grateful to my advisor, Professor Alberto Aliseda, who provided excellent guidance and unyielding encouragement throughout all of my endeavors at the University of Washington. A am also very thankful to Professor Phil Malte and Professor James Riley for teaching me about renewable energy and fluid mechanics which provided me with invaluable knowledge in pursuit of my research goals. This work would not have been possible without the support of the Northwest National Marine Renewable Energy Center as well as the faculty and staff members of the University of Washington Mechanical Engineering Department. Last, I would like to thank my family and friends for their unwaivering support and for always encouraging me to challenge myself.

Chapter 1
INTRODUCTION

1.1 Renewable Energy

As the energy demand throughout the world increases, we continue to drain the available energy stores towards exhaustion. This imbalance gives rise to many current research investigations that focus on finding viable energy alternatives. In the search for new sources of energy, renewable forms are the most desired. These forms can aid in a long term solution to meet the world's growing resource demands and are also often the most environmentally benign, contrasting the carbon and greenhouse gas emitting options of burning oil or coal.

The world has made its strong desire for clean renewable energy tangible by imposing various sanctions, setting goals to provide a large portion of the world's energy demand with renewable resources. In June of 2009 the European Parliament and Council signed its 20-20-20 climate and energy package into law, mandating that by the year 2020, at least 20% of the European Union's energy consumption be provided by renewable resources as well as mandating a reduction in greenhouse gas emissions of at least 20% from 1990 levels [1]. European Union leaders are also proposing even more ambitious targets, contingent on the other major greenhouse gas emitting and energy consuming countries committing to their fair share of reductions.

In the United States, state legislations are also imposing their individual renewable energy targets. As of May 2009, 24 states had Renewable Portfolio Standards in place which require utility companies to provide a certain percentage of their power from renewable energy resources by a targeted date, and another five states have set re-

newable energy goals [2]. Washington State's Renewable Portfolio Standard requires 15% of large utilities electricity production come from eligible renewable energy resources by 2020 [3]. Eligible sources include various forms of solar energy, wind energy, bio-energy, marine energy, and some freshwater hydroelectric improvement projects [4].

In order to meet these energy standards across the globe, research into renewable energy technologies must be pursued. As the energy demand increases and our resource reserves decline, much research is dedicated to finding viable energy alternatives. Wind energy has emerged as a leader of new energy sources, while other options continue to be investigated. More recently, the kinetic energy of water currents in oceans, rivers and estuaries is being explored as predictable and environmentally benign. Tidal flows have been recognized as a potential opportunity to harvest energy that is renewable and clean. Additionally, unlike many other renewable resources, tidal energy is also very predictable. It is estimated the total tidal energy potential of the world is approximately 3 TW with 1 TW in accessible areas for installation of energy extracting devices [5].

1.2 Tidal Energy

Tides are driven by the gravitational effects of the Sun and Moon on the Earth's large bodies of water. The movement of the Sun and the Moon relative to the Earth creates a twice daily rise and fall in the large bodies of waters, generating flows through the tidal channels. In the narrow constricted areas of the channels, the flow has high levels of kinetic energy. Newton's law of gravitation governs these forces on Earth's water bodies:

$$F = G\frac{m_1 m_2}{r^2} \tag{1.1}$$

where F is the gravitational force between two masses, m_1 and m_2 , that are separated by a distance r, with G as the gravitational constant, $6.67 \times 10^{-11} \frac{Nm^2}{kg^2}$.

Despite the much larger mass of the sun, compared to the Moon, the proximity of the Moon relative to the Earth means that the Moon's gravitational forces dominate tides, accounting for approximately 70% of the tidal behavior [5]. As shown in figure 1.1, when the Sun, Moon, and Earth are in line with each other, the gravitational forces of the Sun and Moon pull in the same direction creating a larger tidal range, called spring tides [6]. When the Sun and Moon are at right angles from each other relative to the Earth, their gravitational forces oppose each other, creating a smaller tidal range, or neap tides. Because the movement of the Earth, Sun, and Moon are well understood, their positions relative to each other at any point in time can be determined, allowing tidal heights, and to a certain degree the available energy resource in tidal flows, to be very predictable. It should be noted that due to the complex bathymetry of the tidal basins, a full physical understanding of tidal dynamics is a continued research effort in order to find the most favorable locations for installing marine hydrokinetic (MHK) turbines.

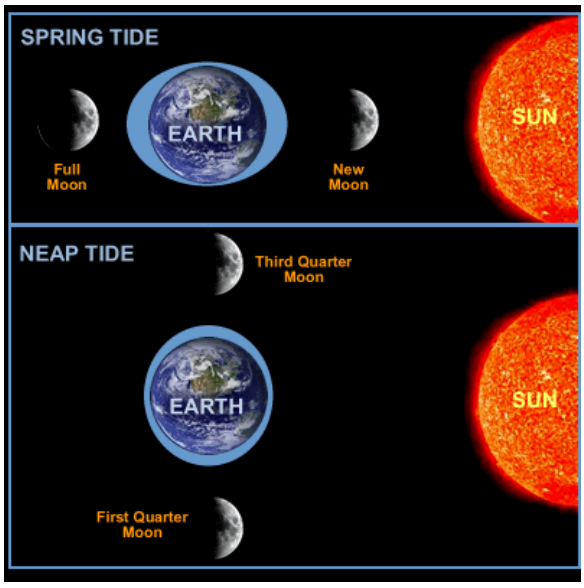

Figure 1.1: Schematic of Spring and Neap tides formation based on the sun, moon, and earth orientation. Source [6]

Though harvesting the energy from tidal flows holds many similarities to harvesting the energy in wind, the hydrodynamic application creates new challenges and involves different physical considerations. Tidal energy industry is still in its infancy. The technology is where the wind energy industry was approximately three decades ago, with many developments to come [7]. Before permitting and installation of devices to harvest this energy can be pursued on a commercial scale, much research must be done to understand the best ways to capture MHK energy efficiently and with the smallest economic and environmental costs.

1.3 Turbines

1.3.1 Classifications

Throughout the development of the wind industry, many concepts for devices to extract the kinetic energy from the flow were created. In the evolution of tidal energy extraction, the industry is in that same early stage where several designs for energy extracting devices are being introduced and investigated. Almost all of these devices can be classified into two types of turbines: axial flow and cross flow, characterized by the direction of the fluid flow relative to the rotational axis as depicted in figure 1.2.

Axial flow turbines are named for having the flow parallel to the axis of rotation. In the wind industry this type of turbine is commonly referred to as a horizontal axis wind turbine (HAWT). Wind is a well understood renewable energy source and harvesting the kinetic energy of the wind is a well-developed technology. Over decades of research and implementation of the technology, the axial flow turbine has emerged as the leader in turbine designs for its ability to most efficiently extract the energy from the flow [8]. At the present time, the wind industry almost exclusively uses axial flow turbines with a few exceptions, such as for small scale residential applications.

Alternatively, cross flow wind turbines (CFWT) and cross flow hydrokinetic turbine

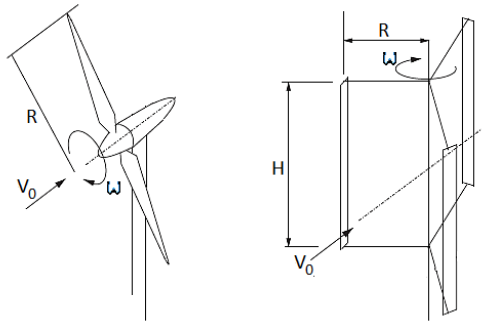

(a) Axial flow turbine (b) Cross flow turbine

Figure 1.2: Axial flow vs. cross flow turbines. Source [8]

(CFHT) have their axis of rotation perpendicular to the flow. Most commonly this type of turbine is implemented with a vertical axis; however, the turbine can also be placed in cross flow with a horizontal axis, often referred to as Transverse Horizontal Axis Water or Wind Turbines (THAWT). While the efficiencies of cross flow turbines are typically less than axial flow turbines, cross flow turbines hold certain advantages that may become more pertinent in the hydrokinetic application: ability to operate in shallow waters with an above-water gearbox and electrical generator, ability to operate in channels with very different depth and widths, the opportunity to stack them as part of "fences" capturing more of the cross section of the flow than possible with a single diameter horizontal axis hydrokinetic turbine, etc.

Tidal energy in its early stages of development and commercialization; on January 23, 2012 the United States Federal Energy Regulatory Commission issued its first pilot project license for tidal energy to Verdant Power for a 1 MW project in New York's East River [9]. The marine environment creates many new variables and additional considerations for energy capture. Many different companies are developing a multitude of concepts for how best to extract the energy from tidal flows. A few examples from some of the commercial leaders are shown in figure 1.3.

(a) Verdant tidal turbine

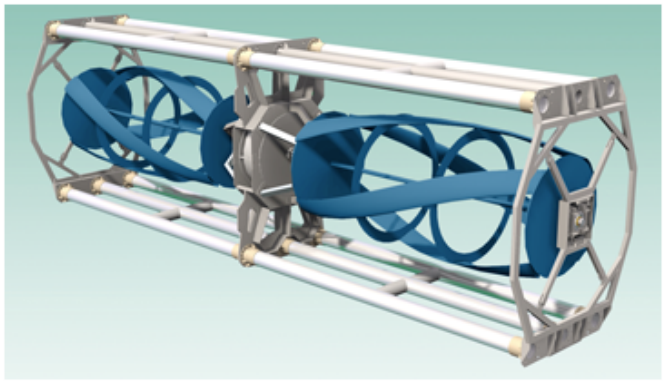

(b) Ocean Renewable Power Company tidal turbine

(c) Openhydro tidal turbine

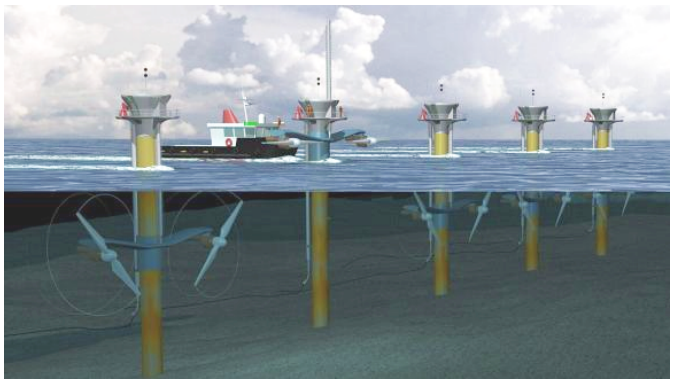

(d) Marine Current Turbines- SeaGen tidal turbine

Figure 1.3: Tidal turbine designs from leading companies. Source: company websites

1.3.2 Advantages of Cross Flow Turbines

Because the physics of axial flow turbines are well understood from research and development in the wind industry, axial flow turbines were a logical starting point for research into marine hydrokinetic turbines; however, cross flow turbines have many potential advantages for the marine application, suggesting we investigate their energy harvesting properties at depth.

The available energy in tidal flows is proportional to the velocity cubed, making viable sites for turbine placement limited to the narrow constricted channels where the velocity is at its greatest and the energy density its highest. The concentrated nature of this resource proposes that optimum packing of turbines within the confinement of a tidal channel is essential to the efficiency and economic feasibility of energy extraction.

The cylindrical shape of the cross flow turbine, lends itself to being easily stacked and arranged in an array, utilizing the limited space. Figure 1.4 shows potential array concepts. The disk shape of axial flow turbines makes them more difficult to arrange in a constricted area without interference. While the cross flow turbine may have a slightly lower power extraction efficiency compared to the axial flow turbine, it can make up the power loss by having a superior turbine power farm arrangement.

It is also suggested that the efficiency of each individual cross flow turbine can actually be increased in the power farm where ducted flow is created by using neighboring turbines. There is a bypass effect that occurs when the fluid flow encounters the high pressure field in front of the turbine, causing some of the flow to follow a path to the sides of the turbine rather than through it, reducing the amount of power extraction [8]. The blockage ratio of the channel can be determined by the ratio of the swept area of the turbines to the channel area normal to the flow. By having a farm of turbines, the blockage ratio is increased, limiting the bypass effect by straightening the flow into a more optimal path.

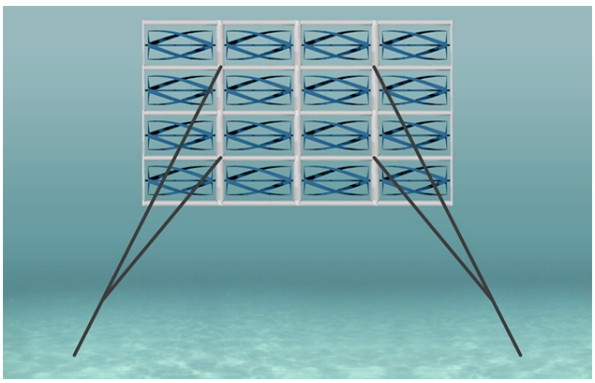

(a) Ocean Renewable Power Company array concept. Source: company website

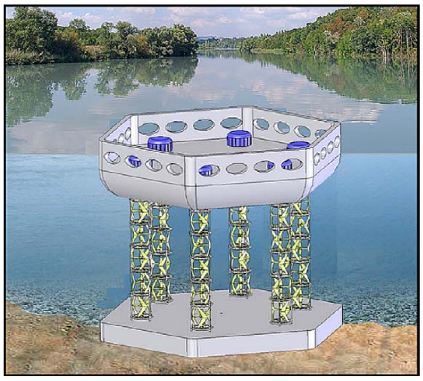

(b) CFWT cluster. Source [10]

Figure 1.4: Potential cross flow water turbine array designs

In addition to working well in the constricted tidal channels, the stacking of cross flow turbines allows them to share a common electric converter reducing equipment and maintenance costs, which in the hydro application can be a very important advantage. The vertical axis type of cross-flow turbines also holds the advantage of being able to work in any direction of flow. This advantage is especially pertinent due to the bi-directional nature of tidal flows, as well as in locations where tidal flows are far from symmetric in ebb and flood resulting in multi-directional velocities over the tidal cycle. With no need for complicated yawing mechanisms on the turbines, once again construction and maintenance costs can be reduced.

Another potential advantage of CFHT is that axial flow turbines typically reach higher tip speeds, making them more prone to cavitation, which reduces the efficiency and can create surface damage [8]. In addition, cross flow turbines are typically configured with smaller part sizes relative to axial flow turbines, making their manufacturing and transportation process less arduous and costly.

Cross flow turbines do have their disadvantages as well. Over recent years, turbine designers have worked to mitigate these issues. The wind industry found that the periodic loading created large vibrational effects that were structurally undesirable; however this periodicity has been limited in new developments for cross flow turbines. The classical cross flow turbine is the Darrieus turbine which has straight blades, creating cyclical effects as the turbine rotates. In recent years the Gorlov turbine, which uses helical shaped blades, and the Achard turbine, which uses delta-shaped blades, have been developed to address the vibrational problems. Examples of these three variations - Darrieus, Gorlov, and Achard - can be seen in figure 1.5. The new designs of the Gorlov and Achard turbines have smoothed the hydrodynamic loading on the blade, limiting the fatigue phenomenon and increasing the life of the turbine. Another known disadvantage of the Darrieus cross flow turbines is its inability to self-start. In addition to limiting vibrational issues, the blade shapes of the Gorlov and Achard turbines also allow self-starting.

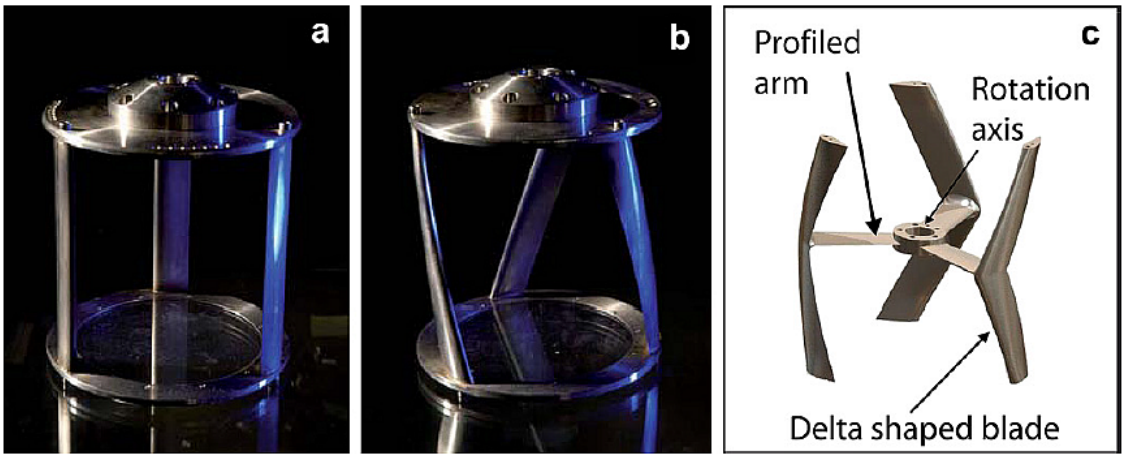

Figure 1.5: Cross Flow Water Turbine examples for a) Darrieus (1931), b) Gorlov (1997), and c) Achard (2004) turbines. Source [10]

1.4 Hydrodynamics of Cross Flow Turbines

1.4.1 Marine Application

There is not yet a comprehensive understanding of turbine behavior for a marine application. While the development of technology for wind turbines, marine propellers, and traditional hydropower turbines has given useful insights into the physics for MHK turbines, there is not a complete overlap for a full characterization of the MHK behavior [11]. Significant differences between marine hydrokinetic turbines and wind turbines include changes in Reynolds number, different inflow conditions, different stall characteristics, and the possibility of cavitation [12].

The power available in the flow for any medium is a measure of the kinetic energy passing per unit time given by

$$P_0 = \frac{1}{2}\rho S_{ref} {V_0}^3 \tag{1.2}$$

where ρ is the density of the fluid, V_0 is the free stream velocity, and S_{ref} is the turbines swept area normal to the flow. For a cross flow turbine

$$S_{ref} = 2RH \tag{1.3}$$

with R and H being the radius and height of the turbine respectively. One key difference between the winds and tidal flows is the typical free stream velocity. Wind speeds are typical around $12\frac{m}{s}$ while tidal flows tend to be closer to $2\frac{m}{s}$ [13]. The power available is proportional to the velocity cubed, making this a significant difference. Another dissimilarity, however, is the density of the fluids. Because the density of water is 832 times that of air, there is comparable power available for a MHK turbine with the same swept area as a wind turbine, with a Reynolds number larger by a factor of 2.5. Comparable swept areas are typically not possible; however, given the cost of installation for MHK as a function of hub height [14], the limitations in depth

for MHK turbines, and the restrictions imposed by environmental and common uses such as shipping or fishing.

1.4.2 Cross Flow Turbine

In addition to accounting for the changes due to the marine environment, the dynamics specific of a cross flow turbine can be quite complex. The flow field is very unsteady and largely three-dimensional. There is much interference between the shed vortices and blades. In addition, dynamic stall behavior is very prevalent as the blade encounters rapidly changing angles of attack throughout its rotation. Despite this complexity, the basic Blade Element Momentum (BEM) theory can serve as a starting point for understanding the flow dynamics.

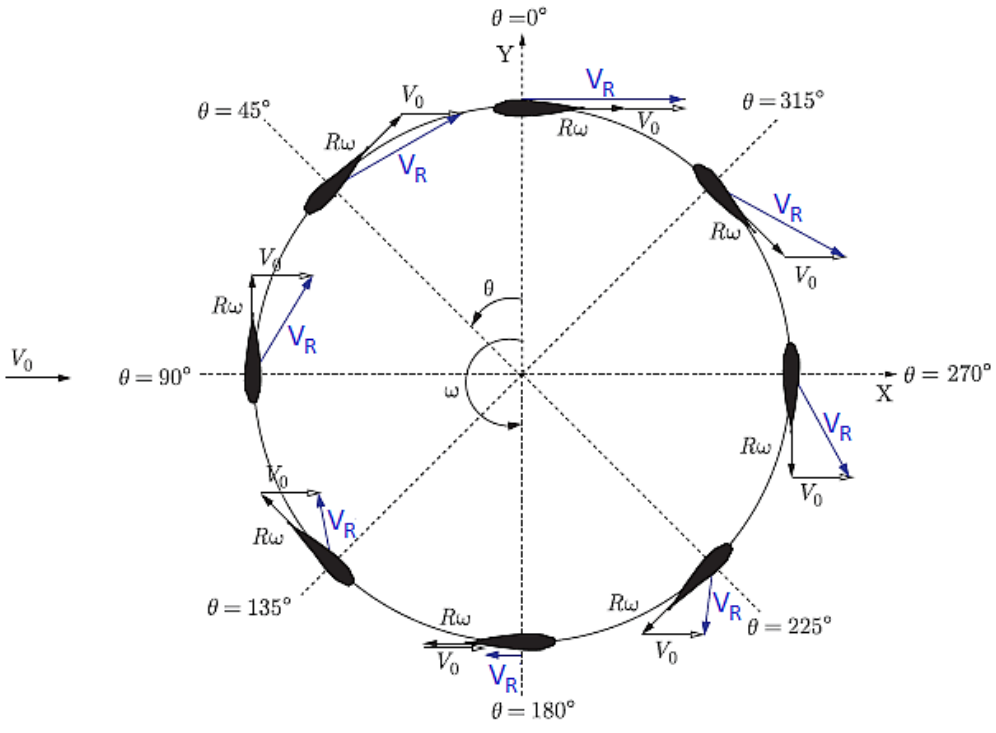

Figure 1.6: Schematic of azimuthal position and velocity triangle. Source [8]

As seen in figure 1.6, the turbine blade position can be described by its azimuthal coordinate θ. As the blade rotates it encounters a resultant velocity made up of the free stream velocity V_0 as well as the tangential velocity $V_\theta = \omega R$ where ω is the angular velocity and R is the radius of the turbine. The resultant velocity for a blade at any azimuthal position can be given by

$$V_R = \sqrt{(V_0 + V_\theta cos\theta)^2 + (V_\theta sin\theta)^2} \tag{1.4}$$

The ratio of the tangential velocity to the free stream velocity is commonly referred to as the tip speed ratio, λ, where

$$\lambda = \frac{\omega R}{V_0} \tag{1.5}$$

The angle of attack as shown in figure 1.7 can also be determined. The angle of attack, α, is a measure of the angular distance between the resultant velocity V_R and the chord line of the blade, which for a cross flow turbine is often the same as the tangential velocity direction. Figure 1.8 shows a plot of the theoretical angle of attack versus azimuthal position for various tip speed ratios. The angle of attack is calculated by

$$\alpha = tan^{-1}\left(\frac{sin\theta}{\lambda + cos\theta}\right) \tag{1.6}$$

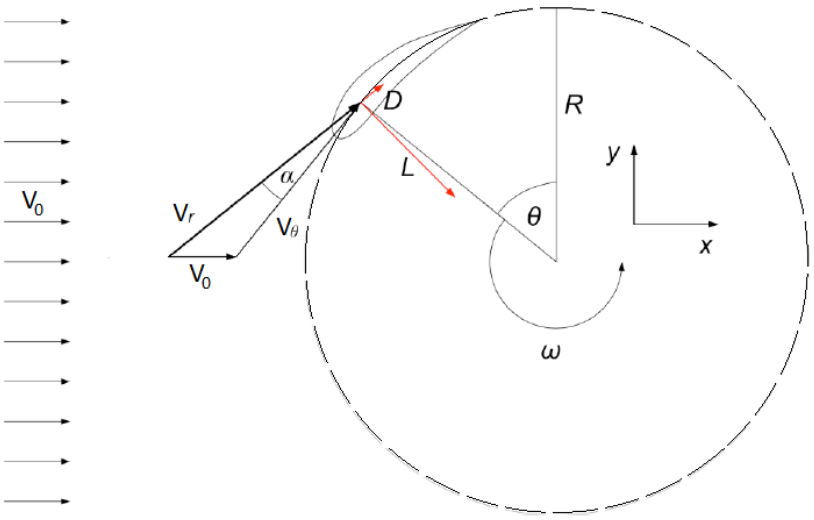

Figure 1.7: Schematic of angle of attack, lift, and drag

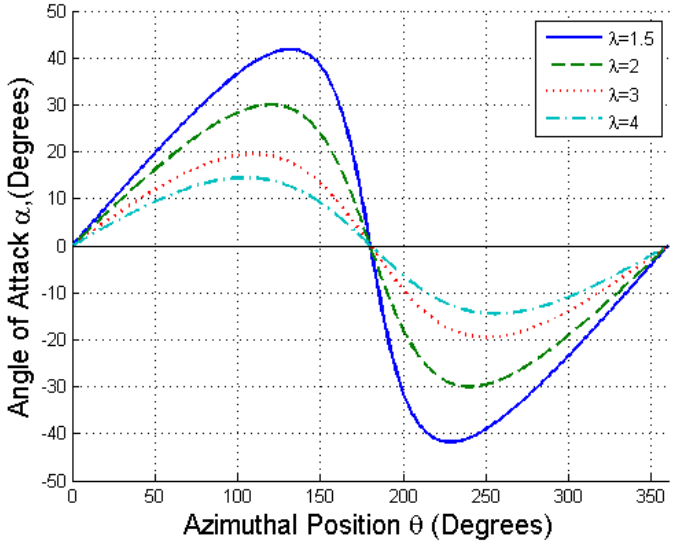

Figure 1.8: Angle of attack vs. azimuthal position

The Reynolds number calculations are also very important for characterizing the flow. There are actually two characteristic Reynolds numbers that should be considered. First there is the Reynolds number determined from the free stream velocity and the blade's chord length c, where ρ is the density and μ is the dynamic viscosity of the fluid.

$$Re_c = \frac{\rho V_0 c}{\mu} \tag{1.7}$$

This Reynolds number gives a general reference for the operating regime of the turbine. It is an adequate description of the flow for a static turbine, but for a rotating rotating turbine the Reynolds number that describes the flow at turbine blade is better characterized by the turbines relative velocity V_R. The relative Reynolds number Re_{rel} can be defined as

$$Re_{rel} = \frac{\rho V_R c}{\mu} \tag{1.8}$$

The relative Reynolds number is dependent on both the angular velocity and the tip speed ratio, as is the relative velocity. Figure 1.9 shows a plot of the theoretical relative Reynolds numbers experienced by the blade at the different azimuthal locations for various tip speed ratios.

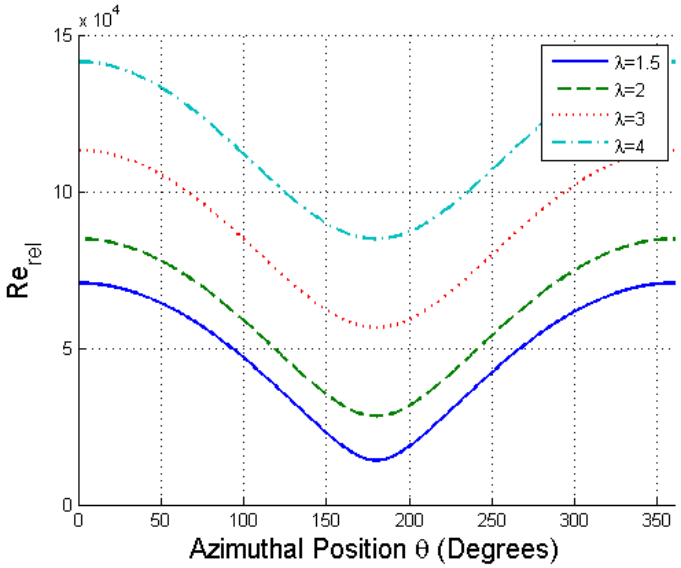

Figure 1.9: Relative Reynolds number vs. azimuthal position

The lift and drag forces, L and D in figure 1.7, on the airfoil are due to the pressure differences and shear stresses along the blade wall and are defined by the drag force being the component in line with the relative velocity vector and the lift force being in the perpendicular direction. In a two-dimensional analysis these forces can be normalized by equations 1.9 and 1.10 as the coefficients C_l and C_d. The coefficients of lift and drag are directly dependent on the the angle of attack as well as the relative Reynolds number.

Coefficient of lift

$$C_L = \frac{L}{\frac{1}{2}\rho V_R^2 c} \tag{1.9}$$

Coefficient of drag

$$C_D = \frac{D}{\frac{1}{2}\rho V_R^2 c} \tag{1.10}$$

BEM theory provides a good basis of the physics for the turbine; however, the complicated nature of the cross flow turbine cannot fully be described. First, there is an issue that on the backside of the turbine (azimuthal positions 180 to 360 degrees)

the oncoming far field velocity is no longer the free stream velocity, but rather some unspecified velocity in the wake from the front side of the turbine that may also contain additional turbulence. Second, there is the issue of dynamic stall where the coefficients of lift and drag for the blade are not only dependent on the angle of attack but also dependent on rate of change of the angle of attack for the particular blade section. This unsteady and very three-dimensional nature of flow for a cross flow turbine makes predicting the flow and power extraction very complex.

The drag and lift forces on the blade create a torque about the turbine axis. This torque is composed of the tangential components of the lift and drag on the blade(s) multiplied by the radius given by

$$T = R(Lcos\alpha - Dsin\alpha) \tag{1.11}$$

The torque for a three dimensional blade(s) can also be effectively described by the coefficient of torque C_T defined as

$$C_T = \frac{T}{\frac{1}{2}\rho {V_0}^2 S_{ref} R} \tag{1.12}$$

The power extracted by the turbine is calculated

$$P = T\omega \tag{1.13}$$

The coefficient of power C_P is a measure of the efficiency of this power extracted from the total power available in the flow. The equations for the coefficient of power and its relationship with the coefficient of torque are given by

$$C_P = \frac{P}{P_0} = \frac{P}{\frac{1}{2}\rho S_{ref} {V_0}^3} \tag{1.14}$$

$$C_P = \lambda C_T \tag{1.15}$$

Chapter 2

BACKGROUND

2.1 Motivation and Goals

Forty years of intense research and development in the wind industry has produced a wealth of information on all fundamental and engineering aspects of flow around Horizonal Axis Wind Turbines. While HAWTs became a well-developed and understood technology, very little attention was paid to cross flow turbines after the first decade of development, when the dominance of HAWTs for utility scale electricity generation was established. As a result, significant gaps in our understanding and modeling capabilities of flow in this type of turbines remain to this day. As described in Chapter 1, cross flow turbines present many advantages in the hydrokinetic application over the traditional axial flow turbines. The recently realized opportunity for cross flow hydrokinetic turbines has ignited interest in understanding the hydrodynamics of CFHT and the development of simulation tools to study the detailed flow around these turbines. With the aid of numerical models, the turbine design as well as the influence of stacking, mooring cables, structural frame, etc. can be analyzed "in-silico" before moving to very expensive and time consuming experiments. Additionally, numerical simulation provides the opportunity to predict environmental effects prior to deployment.

As part of the research for the Univeristy of Washington's National Northwest Marine Renewable Energy Center (UW-NNMREC), the goal of this thesis is to develop a numerical methodology to simulate the performance of a CFHT. With the numerical model we hope to gain a better understanding of the flow dynamics and realize the limitations of numerical simulation for this application. In this context, we used

the recent development of a small scale CFHT turbine at NNMREC to validate this numerical methodology. This small scale development was motivated by a micropower application to power oceanographic instrumentation, including the "Sea Spider" platforms used by NNMREC for the long-term instrument deployments at Admiralty Inlet. The methodology, however, is applicable to full scale turbines with some considerations for the large Reynolds numbers that will be discussed in the section on turbulence modeling.

2.2 Turbine Parameters

In this thesis, we concentrate our efforts on the simulation of a small scale turbine designed within NNMREC and tested in a small cross sectional area water recirculating channel. The turbine design includes four helical blades, each sweeping 90 circumferential degrees. The 360° combined span of the helical blades reduces the total torque of the turbine to essentially a constant value, improving the life of the turbine as well as the self-starting capabilities. The geometrical parameters of the design are given in table 2.1. The NACA 0018 classification indicates the hydrofoil is symmetric and has an 18% width-to-thickness ratio.

Table 2.1: Blade and Turbine Parameters

Blade Profile	NACA 0018
Number of Blades, N	4
Chord Length, c	0.040 m
Radius, R	0.086 m
Height, H	0.234 m

The sweep in the helical blade geometry is given by the inclination angle, ϕ, which is a measure of the inclination of the blade with respect to the horizontal plane. An inclination angle of 90° indicates a straight blade as found in the Darrieus type

turbine. For a turbine with evenly distributed blades, the inclination angle can be calculated by equation 2.1. In general, the closer the inclination is to 90°, the better the efficiency [15]. An additional description of the turbine geometry is the aspect ratio which is the ratio of the turbine's height to the diameter. The micropower turbine design used in this thesis for validation, had an inclination angle, ϕ, equal to 60° that results in an optimum trade off between relatively high efficiency and a reasonable aspect ratio [16].

$$\phi = tan^{-1}\frac{NH}{2\pi R} \tag{2.1}$$

Another important parameter that significantly affects the turbine performance is the solidity ratio, σ, given by equation 2.2. Higher solidity turbines tend to have their peak efficiency operation at lower tip speed ratios [15]. Additionally the solidity ratio can have a large impact on the starting torque, with a higher solidity improving the starting performance. Table 2.2 gives the inclination angle, aspect ratio, and solidity ratio for the turbine modeled in the numerical simulations in this thesis. To improve our understanding of the hydrodynamics of CFHT we performed simulations of a full four-bladed turbine, as well as for a single blade. This latter simulation of just one element, provided us with further insights into the mechanical behaviour of the turbine and the evolution of flow around each blade at rapidly varying angles of attack. The availability of single-blade experimental results to compare against these simulations was a key element in shedding light over the capabilities of the simulation techniques used and the experimental testing conducted.

$$\sigma = \frac{Nc}{2\pi R} \tag{2.2}$$

Table 2.2: Calculated Turbine Parameters

Inclination angle, ϕ	60°
Aspect Ratio	1.4
Solidity ratio, σ, for 1 blade case	0.075
Solidity ratio, σ, for 4 blade case	0.03

2.3 Literature Review

2.3.1 Numerical models

Vertical axis turbines have been of interest for many decades and several methodologies have been developed to numerically predict the performance of these turbines. Numerical models were developed for Darrieus wind turbines but also can be applied in the marine setting. Islam et al. discusses the different models that have been developed including streamtube momentum models, the Vortex model, and the Cascade model [17].

Momentum models equate the forces on the blades with the change of streamwise momentum of the fluid. In 1974, Templin [18] developed the single streamtube model in which the entire turbine is enclosed within one streamtube. In 1975, Strickland [19] improved upon this model with the multiple streamtube model in which the swept volume of the turbine is split into independent parallel streamtubes for the calculation. These allowed for the different values of the hydrodynamic forces, lift and drag, at different angles of attack that act on the blades at different positions along their circumferential trajectory to be taken into account in the momentum balance for each streamtube. In 1981, Paraschivoiu [20] introduced another improvement called the double-multiple streamtube model in which a calculation is done separately for the upstream and downstream half cycles of the turbine to take into account the effect of the momentum deficit created from the upstream half cycle on the downstream

half. Typically, these streamtube models can predict the performance of the turbine reasonably well with limited computation time. They are stationary models and take into account the time-averaged cumulative effects of the rotating blades. Unfortunately, the models do tend to break down for higher tip speed ratios and also for high solidity ratios. Figure 2.1 shows schematics of these variations of the streamtube momentum model.

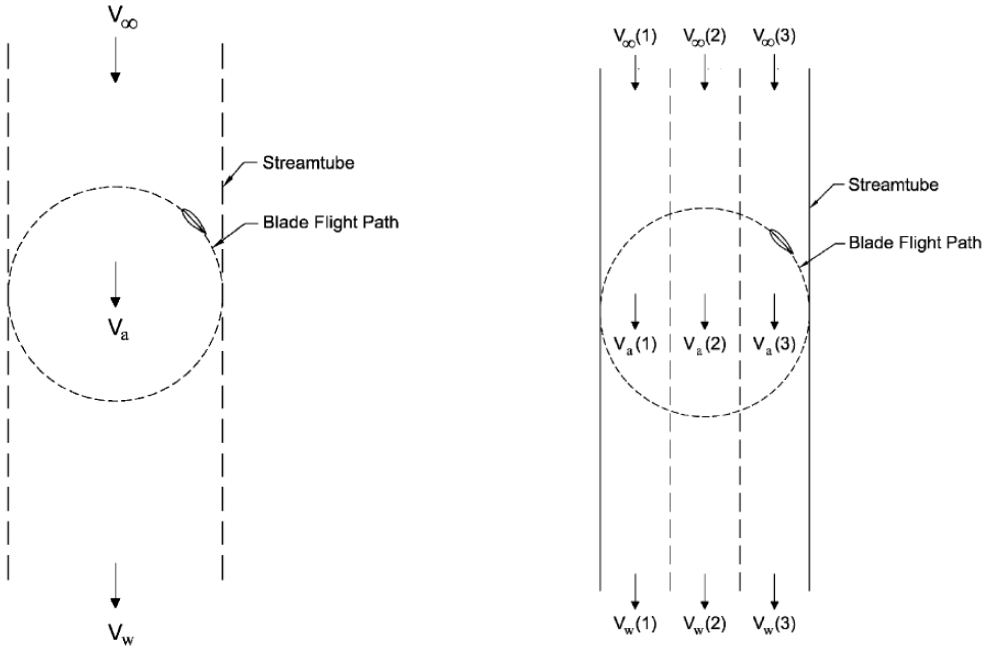

(a) Single streamtube model

(b) Multiple streamtube model

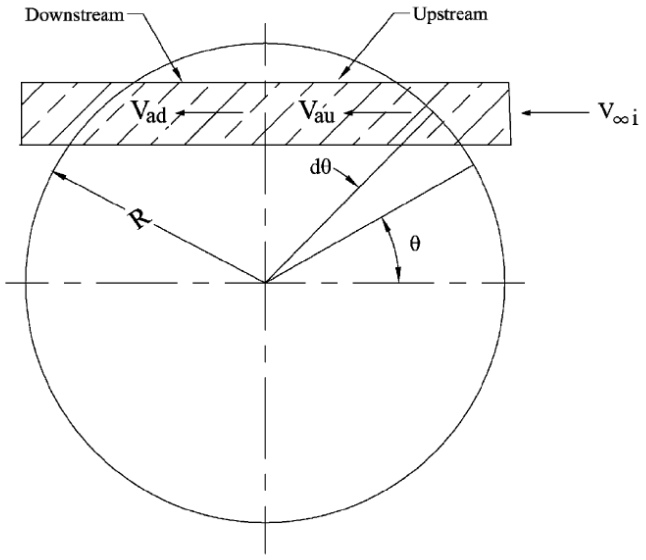

(c) Double-multiple streamtube model

Figure 2.1: Schematics of streamtube models. Source [17]

Vortex models, based on Prandtl's lifting line theory, are potential flow models that calculate the velocity around the turbine using the vorticity on the turbine blades and in the wake of the blades. The turbine blades are represented by a vortex filament (also called a lifting line) as shown in figure 2.2 and the strength of the vortex is determined using airfoil coefficient datasets, the calculated relative flow velocity, and the calculated angle of attack. In 1975, Larsen [21] first applied the lifting line idea from aerodynamics to wind turbines, creating the first Vortex model, and in 1979 Strickland et al. [22] developed a three-dimensional vortex model that also took aerodynamic stall into account. Other advances have been made to the model such as incorporating dynamic stall effects, added mass effects, and flow curvature. Vortex models are more accurate than momentum models but require greater computational costs.

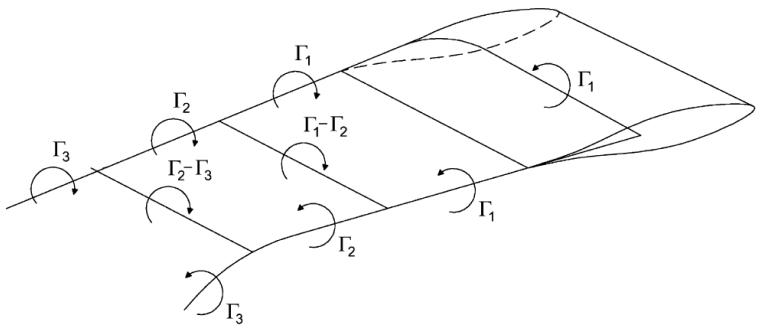

Figure 2.2: Schematic of Vortex model blade representation. Source [17]

The Cascade model, proposed by Hirsh and Mandal [23], represents the blades by positioning them equally spaced on a plane surface, with blade to blade distance equal to the turbine circumferential length divided by the number of blades, as shown in figure 2.3. The relationship of the wake velocity and the induced velocity is determined for the upstream side by

$$\frac{V_{au}}{V_0} = \left(\frac{V_e}{V_0}\right)^{k_i} \tag{2.3}$$

and for the downstream side by

$$\frac{V_{ad}}{V_e} = \left(\frac{V_w}{V_e}\right)^{k_i} \tag{2.4}$$

where V_{au} and V_{ad} are the induced velocity on the upstream and downstream sides of the turbine respectively and V_e and V_w are the velocity in the wake for the upstream and downstream sides respectively. The value for the exponent k_i is found empirically from fitting to experimental results given by

$$k_i = 0.425 + 0.332\sigma \tag{2.5}$$

where σ is the number of blades times the chord length divided by the radius.

The model predicts performance for low and high solidity turbines more accurately than the conventional momentum model and does not have convergence issues for high tip speed ratios or high solidities. With additional corrections of dynamic stall and flow curvature with blade pitching, the predictions are comparable with those of the complex dynamic Vortex model.

While these earlier models do a reasonable job predicting the flow for a Darrieus turbine, the more recent developments in blade geometry design such as the Gorlov and Achard turbines cannot be accurately predicted by these simple methods. The relative simplicity of the hydrodynamics in this methods does not take into account complex viscous phenomena such as stall and blade-wake interactions, as well as tur-

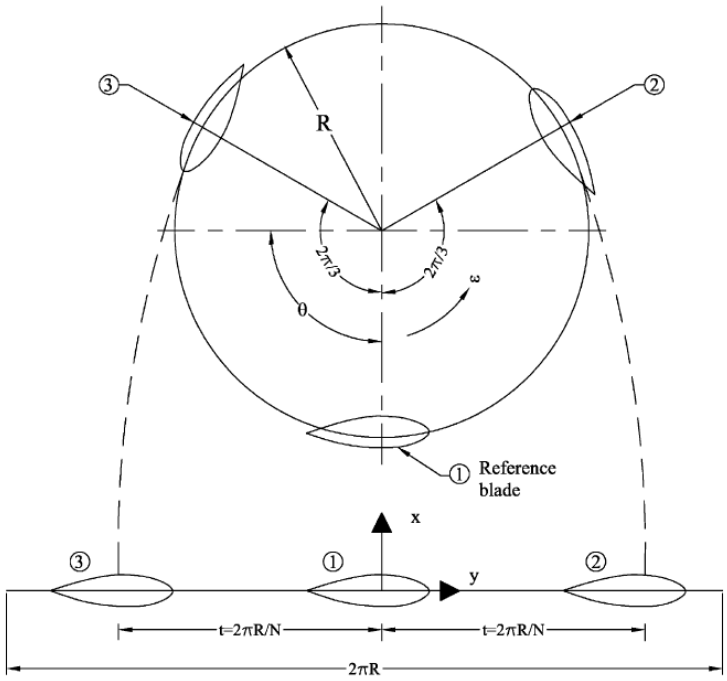

Figure 2.3: Schematic of Cascade model. Source [17]

bulence and variability in the flow incoming into the turbine. The Marine application of energy extracting turbines has led to renewed interest in Cross Flow Turbines, leading to more recent efforts to adapt these models to more complicated blade designs [16].

2.3.2 Computational Fluid Dynamics Macroscopic Coupled (CFDMC) Model

In addition to improvements to simplified numerical models, analysis of Cross Flow Turbines has also turned to Computational Fluid Dynamics (CFD) simulation in recent years. The numerical models described previously have to make several assumptions and corrections to account for the full three-dimensional, turbulent flow dynamics around the turbine blades. CFD eliminates the need for many, but not all, of these assumptions. It also has the advantage of resolving the full time-dependent

flow field, allowing for better understanding of the flow at the blade wall as well as in the wake of the turbine. CFD does, however, come with a much greater computation cost.

Antheaume et al. proposed a new model for studying the Darrieus turbine that utilizes the benefits of CFD without the need for modeling the full blade geometry. This model will be referred to as the CFD-Macroscopic Coupled (CFDMC) model [8]. The model is very similar to the Virtual Blade Model (VBM) proposed by Zori and Rajagopalan to simulate a helicopter rotor system [24]. VBM has been implemented with success for modeling Horizontal Axis Hydrokinetic Turbines [25] [26]. In this model, a steady state formulation is used to simulate the time-averaged cumulative effects of the rotating blades. The effect of the turbine blades is modeled through source terms in the momentum equations placed in the volume swept by the rotating blades. For the cross flow turbine, the swept volume is represented by an annular cylinder with thickness equal to the blade, centered about the turbine axis of rotation. The momentum source term is determined by a Blade Element Theory calculation that is dependent on the lift and drag coefficients for the different sections along the turbine blade. These coefficients must be known from experiments a priori for that particular blade profile, angle of attack, and Reynolds number. The instantaneous lift and drag forces are time-average and cell volume-weighted. A steady state solution is reached after the iteration procedure converges.

The CFDMC model makes the assumption that the ratio of the chord length of the blade to the radius of the turbine is much less than one and that the number of blades is small enough that the blades are not too close together, limiting the turbine parameters the model can be used for. The model also has a drag correction C_{D_o} applied to account for the additional drag due to other rotating parts of the turbine. An application of the model for a three bladed Darrieus wind turbine operating at a $Re_c \sim 150{,}000$ has been validated with experimental data from Sandia National Laboratory [27]. Good agreement was found for the three solidity ratios

simulated ($\sigma = 0.039, 0.035, 0.028$) for tip speed ratios above the value corresponding to the maximum C_p (about $\lambda = 4.5$). The "good quality of the comparison" requires adjusting the C_{D_o} value in a purely empirical fashion. Their model under-predicts the performance compared to the experiment at low tip speed ratios (below $\lambda = 4$) which is attributed to the dynamic stall phenomenon. It is suggested this could be accounted for with another empirical correction.

After developing the validated model, additional simulations were run for cases with multiple stacked turbines as well as several turbines in a row. They showed that the difference between a two-dimensional case (simulating an infinitely tall turbine) and a a three-dimensional simulation of a single turbine is a 6% increase in efficiency. When a three-dimensional case with eight turbines stacked vertically was compared to a the single three-dimensional turbine, the difference in efficiency was 4% in favor of the stacked turbines. This suggests that tip effects are minimized when turbines are stacked in the direction of the axis of rotation, leading to better performance.

Two-dimensional simulations for a barge configuration of five turbines across a channel showed an increase in efficiency as the spacing between the turbines was minimized. This improved performance is related by the blockage ratio of the turbine array in the channel and was explained by the "velocity streamlines straightening effect" caused by this turbine configuration, as can be seen in figure 2.4.

Zannette et al. used the two-dimensional CFDMC model to compute pressure fields in a structural analysis on CFHT including Darrieus, Gorlov, and Achard turbines as well as a turbine with a newly proposed trapezoidal-blade shape [10]. Only straight-bladed Darrieus turbine pressure fields are obtained from the analysis because sweep and chord length variation are not accounted for in the applied coefficients of lift and drag and there is no span wise flow in the 2-D simulation. The authors made significantly simplifying assumptions in order to calculate pressure fields and hydrodynamic loading on the various blade shapes, with the recognition that they "maximized the resultant force and could be considered as an upper bound, providing a critical case

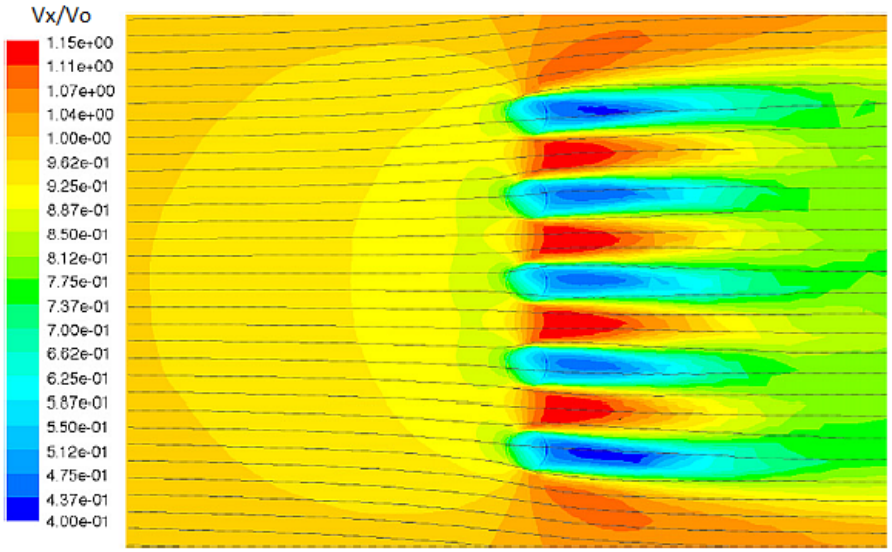

Figure 2.4: Straigtening effect from a tidal turbine barrage. Source [8]

for mechanical analysis."

In the two previously described applications of the CFDMC model, tabulated coefficients of lift and drag are utilized from experiments on a straight blade airfoil, meaning that the model represents a Darrieus turbine. Coefficients of lift and drag including 3D effects could be determined from high fidelity CFD simulations, such as the technique used in this thesis as presented in Chapter 3, where the fully three dimensional flow in the helical blade geometry is actually modeled. Experimental data could provide the same type of three dimensional lift and drag information, if a physical prototype was available. These 3D-flow-based coefficients could then be used as seed data for the CFDMC model to extend studies to a much wider range of operating parameters, with the benefit of the CFDMC model's fast turn around and low computational requirements.

The CFDMC model is shown to provide a very promising methodology to perform turbine power farm analysis as well as structural analysis of different blade types.

By eliminating the need to model the actual blade geometry, computational expense as well as mesh design efforts are significantly reduced. A disadvantage is that the coefficients of lift and drag for the blade must be known a priori as well as an empirical adjustment to the drag correction C_{D_o} must be made to predict performance. Transient effects are disregarded in the model and instantaneous performance and flow characteristics cannot be calculated.

2.3.3 Sliding Mesh Computational Fluid Dynamics Technique

An alternative to simplified models that represent the turbine blades by equivalent forces or vortex filaments, is the sliding mesh technique in a full CFD simulation. This technique uses a highly detailed computational mesh around the geometry of the turbine blades, implementing the physical no slip condition on the blades solid surface. The sliding mesh technique has been employed successfully on two-dimensional simulations that have appeared recently in the literature [28–30]. In this technique, a transient formulation is used to compute the full three dimensional Reynolds Averaged Navier Stokes equations in the channel and around the turbine. At each time step, an inner domain containing the turbine blades rotates relative to an outer stationary domain. The transient solution, as well as the need to calculate the boundary layer flow on the blades and at the interface between the stationary and rotating domains, leads to additional computational costs relative to the CFDMC model. The blade geometry must be modeled leading to a more complicated discretized domain as well as greater computational requirements. This model, however, requires no tabulated coefficients of lift and drag or empirical correction factors. This, together with the calculation of transient effects, represent the most important advantages of this methodology in the understanding of CFHT turbine hydrodynamics and performance. Flow fields at the blade wall are calculated in detail, allowing us to understand the complex interactions of the flow around the blades at rapidly changing angles of attack and in the presence of wakes from other blades. A complete description for the sliding mesh technique

methodology is given in Chapter 3.

In 2005, Maitre et al. [28] conducted two-dimensional simulations for an isolated airfoil and used the sliding mesh technique to simulate a two bladed rotating turbine. The results were compared with experiments for a Darrieus turbine. For the isolated airfoil there was a discrepancy between the simulation and the experiment, coming from the model of flow in the stalled region. The experiment had a measured static stall angle of 9° while the simulation yielded a 12° stall angle. The simulations underestimated the drag and over predicted the lift in the stall region. They suggested that this discrepancy is a result of limitations in the RANS closure model associated with: the laminar part of the boundary layer, the roughness of the blades, and the turbulence intensity of the inflow. For the rotating turbine, a plot of the coefficient of torque for a single blade versus azimuthal position also showed the numerical results overestimating the experimental values, while following the same qualitative behaviour of the torque curve.

In 2009, Consul et al. [29] performed simulations of flow over a rotating NACA 0015 blade at $Re_c = 3.6 \times 10^5$ and compared with experiments. They found limitations in the simulation results due to the difficulty that the Reynolds Average Navier Stokes equations have in modeling the boundary layer laminar to turbulent transition that is present in this regime of low to moderate Reynolds numbers. The simulation showed static stall occurring 2° later in than in the experiment with an over-prediction in the coefficient of lift by around 20%. They suggested that other models could be applied to accurately compute the transition for a static blade; these models, however, would not be suitable for the dynamic flow environment of a rotating CFHT where turbine blades see a continually changing incidence angle. To evaluate dynamic torque, Consul et al. performed two-dimensional simulations with the sliding mesh technique for two-bladed and four-bladed turbines, with solidities of 0.019 and 0.038 respectively using the same Reynolds number operating range of $O(10^5)$. They found that increasing the number of blades led to an increase in the maximum power coefficient from 0.43

to 0.53. Increasing the number of blades shifted the peak of the power curve to a lower range of tip speed ratios. This shift was explained by more blades (and hence higher solidity) leading to a higher flow impedance, which reduced streamwise flow velocity through the turbine. Detailed flow fields of the blade wall region for several azimuthal positions are provided in the analysis. No experimental results are given for validation of the dynamic torque results.

Lain et al. [30] worked to develop a sliding mesh model for a 2-D model of a three bladed Darrieus-type turbine. They performed a complete mesh and time-step independence study. Curves for the coefficients of torque and power versus tip speed ratio were evaluated. Validation was provided, although by just one experimental data point at $\lambda = 1.745$, showing good agreement with the simulation.

Also in 2010, Li and Li [31] developed a similar sliding mesh model to study the effect of solidity ratio, blade profile shape, and number of blades on the performance of the Darrieus turbine. They analyzed both the static and dynamic performance of the different turbines. For the static torque performance, they showed that increasing the solidity led to an increase in the average static torque. For the rotating turbine, it was found that larger solidity led to a higher maximum power with a shift to a lower tip speed ratio. It was also found that further increases of the solidity ratio eventually caused a decrease in the power coefficient. For two cases with the same solidity, the combination of chord length and number of blades also had significant effect on the performance. Both cases had similar performance for tip speed ratios $0 < \lambda < 2$ and reached its maximum C_p at $\lambda = 3$, but for tip speeds of $\lambda > 2$, the turbine with four blades and smaller chord length significantly outperformed the turbine with two blades and the larger chord length, with maximum C_P of 0.011 and 0.075 respectively. No validation results were presented for this study.

Sun and Zhang [32] also performed CFD analysis with a sliding mesh model to search for optimum blade profiles. They found that symmetric airfoils had a higher efficiency than cambered ones at large tip speed ratios, and also that an increase in the airfoil

thickness improved performance at all tip speed ratios. While these findings are not trivial to understand, the paper does not go into depth in explaining the results. Experimental validation was again not provided.

CFD analysis of cross flow turbines has only been investigated on limited occasions, but its benefits have been realized. While the two-dimensional simulation of the sliding mesh technique available in the literature provide valuable insight into the operation of cross flow turbines, the problem is over simplified. While providing some insights with significantly lower computation requirements, two dimensional simulations lack the ability to fully simulate the physical phenomena that is influenced by the highly three-dimensional flow of modern helical CFHTs. Modeling in two dimensions simulates an infinitely long blade, resulting in higher efficiencies. It also eliminates the effects of three dimensional flow in the span-wise direction. Additionally, capturing the geometry and flow for a helical or delta blade is impossible in two dimensions. The smoothing of the torque loads on the turbine due to having a sweeping blade such as in the Gorlov turbine cannot be simulated with a two-dimensional model.

A novel study has been published by Castelli and Benini [33] in early 2012 employing the three-dimensional sliding mesh approach to study the effect of inclination angle for flow over a single rotating blade. An inclined straight bladed case served as the study's validation model, however no comparisons with experiments were provided. The analysis provides preliminary results for flow over a helical blade. The authors point out, however, that in changing the blade inclination angle, the blade profile was also changed, so only a limited comparison of the different inclination angles can be made. It is also noted that the three-dimensional mesh utilized a conversion to polyhedral mesh elements which is "a very resource intensive process" and that the total CPU time was "20 days for each simulation."

Two-dimensional analysis of cross flow turbines present in the literature has shown some important features of the flow and performance of this type of Marine Hydrokinetic Turbines, with the added benefit of limited computational requirements. How-

ever, to capture the flow for a helical bladed turbine accurately, a three-dimensional sliding mesh approach is necessary. This is the methodology developed and employed in this thesis. The methodology and results are discussed in the next two chapters.

Chapter 3

METHODOLOGY

Computational Fluid Dynamics (CFD) is becoming increasingly more popular as a tool for studying flow over both wind and marine hydrokinetic turbines. It has the advantage of being able to resolve the full flow field as well as limiting the assumptions needed in calculations. CFD requires additional computational expense compared to other numerical methods such as potential flow codes; however, with continually increasing computing capabilities, CFD has become a viable option for studying these flows under industrially relevant conditions.

3.1 Renolds Average Navier Stokes Equations

Turbulent flows contain velocity fields that are chaotically fluctuating over a large range of temporal and spatial scales. While direct numerical simulation is possible, capturing these fluctuations requires a highly resolved flow field and is very computationally intensive. The Reynolds Averaging approach is a very popular alternative in CFD for modeling turbulent flow fields. In Reynolds Averaging the variables in the Navier Stokes equations are decomposed into their mean and fluctuating components, known as Reynolds Decomposition [34]:
Reynolds decomposition of velocity

$$\vec{U} = \overline{\vec{U}} + \vec{u\prime} \tag{3.1}$$

Reynolds decomposition of a scalar variable

$$\phi = \overline{\phi} + \phi\prime \tag{3.2}$$

The resulting equations from the decomposition are known as the Reynolds-average Navier-Stokes (RANS) equations. The continuity equation and the momentum equations for incompressible flows become:

Conservation of mass

$$\nabla \cdot \overline{\vec{U}} = 0; \quad \nabla \cdot \vec{u\prime} = 0 \tag{3.3}$$

Conservation of momentum

$$\frac{D\overline{U_i}}{Dt} = \nu \nabla^2 \overline{U_i} - \frac{\partial \overline{u_i\prime u_j\prime}}{\partial x_j} - \frac{1}{\rho}\frac{\partial \overline{p}}{\partial x_i} \tag{3.4}$$

Equations 3.3 and 3.4 are the equivalent of the instantaneous Navier-Stokes equations using the time-averaged variables, however an additional term appears in the momentum equations $\overline{u_i\prime u_j\prime}$ known as the Reynolds Stress. This term creates nine additional unknowns, necessitating a turbulence closure model to solve the system of equations. Numerous turbulence closure models have been developed, while alterations and improvement efforts continue. Most commonly used, are the two-equation turbulence models, k-ϵ and k-ω, in their standard forms as well as their variations.

3.2 Turbulence Closure Models

Developed by Jones and Launder[35], the k-ϵ model is the most widely used turbulence closure model in commercial CFD codes [34]. It has been shown to adequately predict free shear flows, but encounters difficulties in resolving wall bounded flows and adverse pressure gradients. There is also an associated numerical stiffness of the equations when integrated through the viscous sublayer. To address this problem for boundary layer flows, Wilcox[36] developed the k-ω turbulence closure model, which has an improved ability to treat the viscous near wall region as well as streamwise pressure gradients. This makes it a more accurate and robust model for flows that are significantly determined by wall effects. A shortcoming of the k-ω model is that the results depend strongly on the free-stream vorticity values that are specified outside the shear layer.

In an effort to simultaneously capture the accuracy and robust qualities of the k-ω model in the near-wall region and the advantages of the k-ϵ in the far field, Menter developed the Shear Stress Transport k-ω (SST-kω) turbulence closure model [37]. The standard k-ω was modified to be insensitive to the free-stream vorticity values and to improve the predictions of separated flows [38]. The SST-kω model is based off of the k-ω model but also utilizes the k-ϵ model in a transformed k-ω formulation. This transformation allows a blending function to be used in which the two models are applied together [39]. The blending function has a value of 1 (fully standard k-ω modeling) in the near-wall region and then transitions to a value of 0 (only k-ϵ model activated) far from the wall.

This blending of k-ω and k-ϵ makes the SST-kω model superior for many types of flows, including flows past an airfoil or hydrofoil. Because of this improved accuracy, it has become commonly accepted in CFD modeling for wind and marine hydrokinetic turbines to use the SST-kω model as an appropriate method for turbulence closure [29, 30, 33] . The simulations for the research in this thesis have all been performed solving the RANS equations with the SST-$k\omega$ turbulence closure model using the commercial software ANSYS FLUENT v12.0. The turbulence model was applied with no changes to the default parameter settings provided by ANSYS FLUENT.

3.3 Near Wall Modeling

In addition to choosing a turbulence model that is well suited for the particular application of interest, it is important to represent the near-wall region in an appropriate manner, as walls have a significant impact on the flow. Specifically, the high shear imposed by the no-slip wall boundary condition must be well represented in the solution of the velocity at the wall. The turbulence, however, is also affected by the presence of the walls. Very close to the wall, viscous damping and kinematic blocking reduce the tangential velocity and normal fluctuations respectively [39]. In the outer part of the near-wall region, the large gradients in mean velocity lead to significant

production of turbulent kinetic energy that is transported into the free stream.

This near-wall region, where the solution variables have large gradients, is very influential in determining the mean flow characteristics but is also the most important source of mean vorticity and turbulence. Because these physical transports occur on very small scales relative to other length scales in the domain, it is necessary to have a high resolution mesh at the wall for an accurate solution. Creating an accurate numerical representation of the near-wall region is vital to successfully simulating wall-bounded flows.

The near-wall region can be separated into three sublayers as shown in figure 3.1. In the innermost layer, known as the viscous sublayer, the molecular viscosity dominates the resulting momentum and heat or mass transfer. In the outer layer, the fully turbulent region, turbulence significantly affects the flow. Between these two regions is the buffer layer. In this region, both molecular viscosity and turbulence are equally important (section 7.1.3 in [34]). In figure 3.1, y^+ ($y^+ = \frac{u_\tau y}{\nu}$) is the non-dimensional wall distance defined in terms of the wall friction velocity and fluid viscosity.

Modeling the near-wall region can be accomplished by two different approaches. In one method the viscous sub-layer is completely resolved by the mesh, referred to as the "near-wall model" approach. In the other method the viscosity-affected inner region consisting of the viscous sublayer and buffer layer is not resolved. Instead, wall functions based on the logarithmic law of the wall are used to model this zone between the wall and the fully-turbulent region. This method is named the wall function approach. These two different types of near-wall modeling approaches are depicted in figure 3.2.

The level of refinement needed for each of the modeling approaches is determined by the y+ value:

$$y^+ = \frac{u_\tau y}{\nu} \tag{3.5}$$

y is the nearest distance to the wall, ν is the kinematic viscosity of the fluid, and u_τ

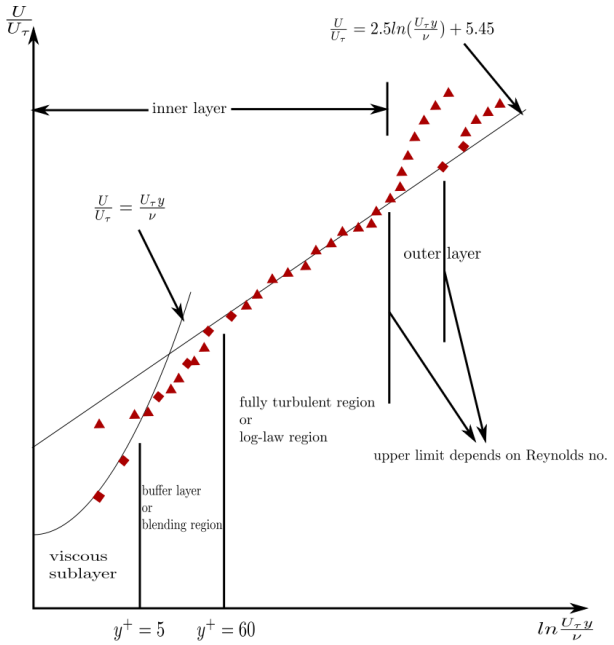

Figure 3.1: Three distinct divisions inside the near wall region. Source [39]

is the friction velocity:

$$u_\tau = \sqrt{\frac{\tau_\omega}{\rho}} \tag{3.6}$$

For the wall function approach, the nearest node to the wall in the mesh should be at a distance y^+ in the range of $30 < y+ < 300$. The y^+ value is solution-dependent, and at times it can be difficult to attain a y^+ value in this range at all locations on the wall. The near-wall model approach requires mesh nodes at very close distances to the wall, $y^+ \sim 1$. Because the mesh for the wall function approach is not as refined, it has significantly less computational costs and is the desired approach when applicable. It provides a sufficiently accurate solution for most high-Reynolds number flows; however, in low-Reynolds number flows the underlying assumptions in the wall functions may no longer be valid. The simulations in the current research occur at a Reynolds number of approximately 3×10^4, a relatively low-Reynolds number flow, therefore both the wall function approach and near-wall model approach are

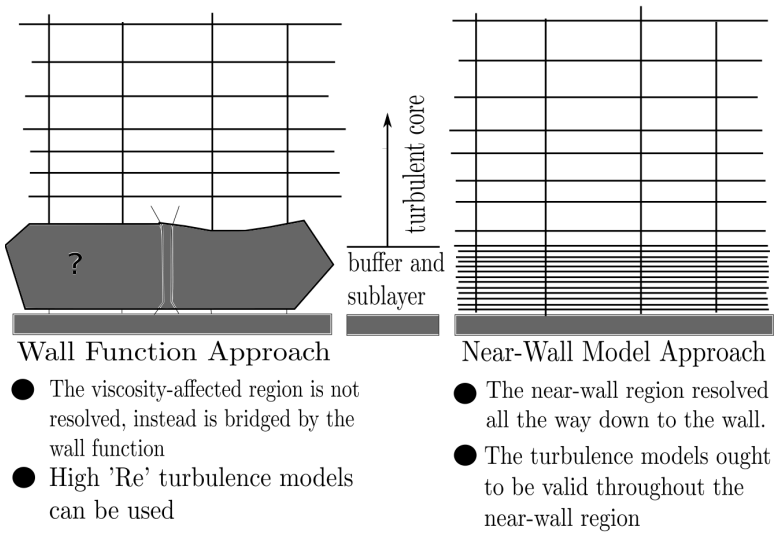

Figure 3.2: Schematic of wall function and near wall model approach. Source [39]

investigated.

3.4 Sliding Mesh Model

In order to simulate a rotating turbine through the flow field, the sliding mesh model technique is applied. The channel domain is split into two cell zones. First, there is an inner cylinder which includes the blade(s) of the turbine. This zone rotates a specified amount for each time step of the simulation. The second zone is stationary and consists of the rectangular channel surrounding this inner cylinder as shown in figure 3.3. Where one cell zone meets the adjacent cell zone is the mesh interface, along which these two zones move relative to each other.

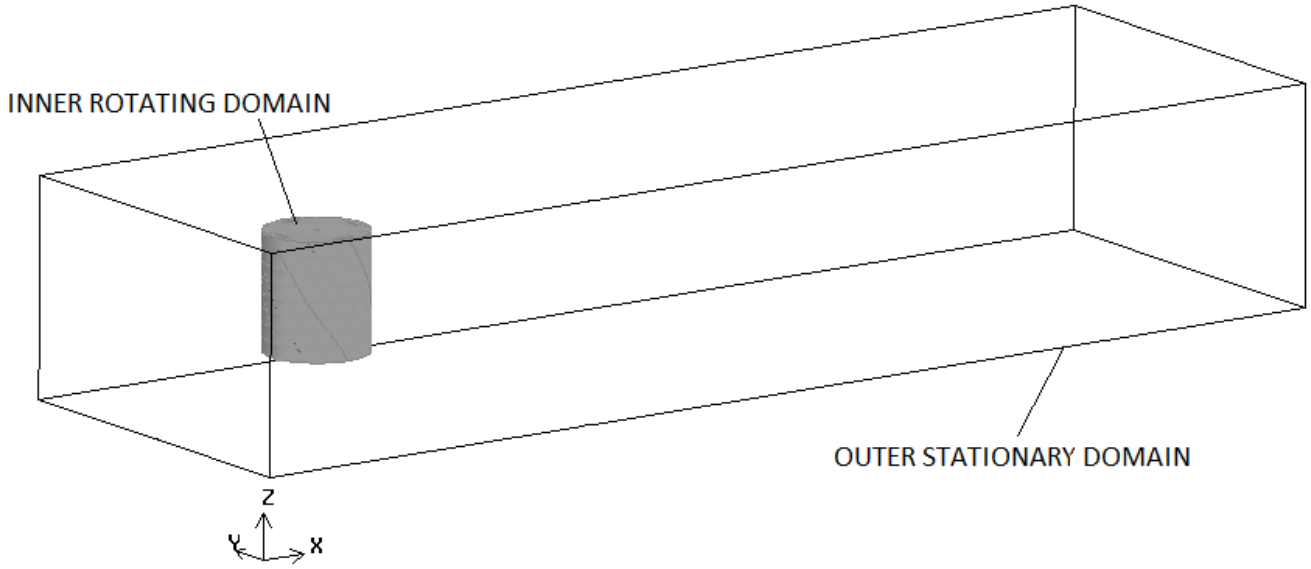

Figure 3.3: Stationary and rotating domains.

The motion of the moving zone is tracked relative to the stationary frame and no moving reference frames are needed, simplifying the flux calculations across the zone interface. The sliding mesh technique allows the unsteady flow field to be computed. It is the most accurate method for simulating flows in multiple moving reference frames, but also the most computationally demanding [40].

As the two cell zones slide relative to each other, the alignment of the cell nodes is not required, creating a non-conformal boundary. To solve the flux across the non-conformal boundary at each time step, ANSYS FLUENT computes the intersection between the interface zones. An example of a non conformal boundary is shown in figure 3.4. The interface zones are defined by the faces A-B and B-C on one side with D-E and E-F on the other. The intersection of these faces creates faces a-d, d-b, b-e, e-f, and f-c. Calculating the flux into zone III can then be determined at each time step using faces d-b and b-e instead of the original faces of the cells. At each time step these intersections are recalculated for the new position and the flux is determined.

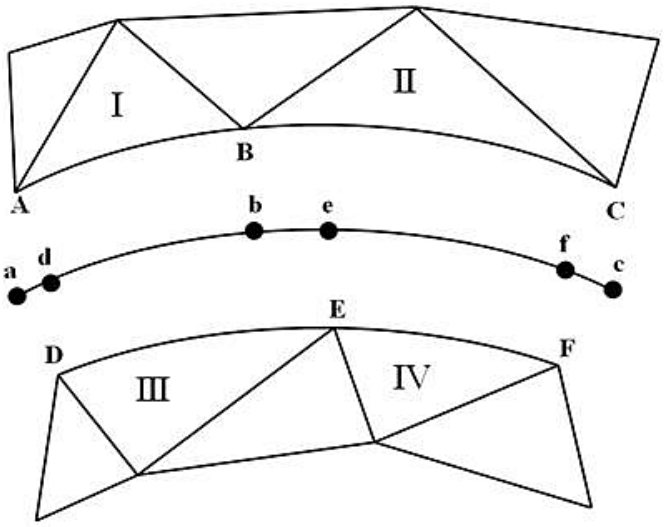

Figure 3.4: Schematic of non-conformal interface.

3.5 Computational Domain and Boundary Conditions

The Channel Domain was created to match the dimensions of the flume in length and width, as well as to match the water height from the experiments. After preliminary modeling, it was proved that a shorter distance from the inlet to the turbine axis could be modeled without altering flow conditions, reducing computation needs. In order to provide the opportunity for more extensive wake analysis, the domain behind the turbine was extended. Figure 3.5 shows the new channel domain with the altered distance from the inlet to the turbine axis as 4.4R and for the wake as 23.6R (compared to the actual dimensions of 13.4R and 13.4R respectively), with R being the radius of the turbine.

The bottom and side walls of the flume were modeled as no-slip walls. The free surface of the water was modeled as a zero-shear wall. This was assumed as a valid boundary condition because the froude number, which is a ratio of the kinetic and gravitational

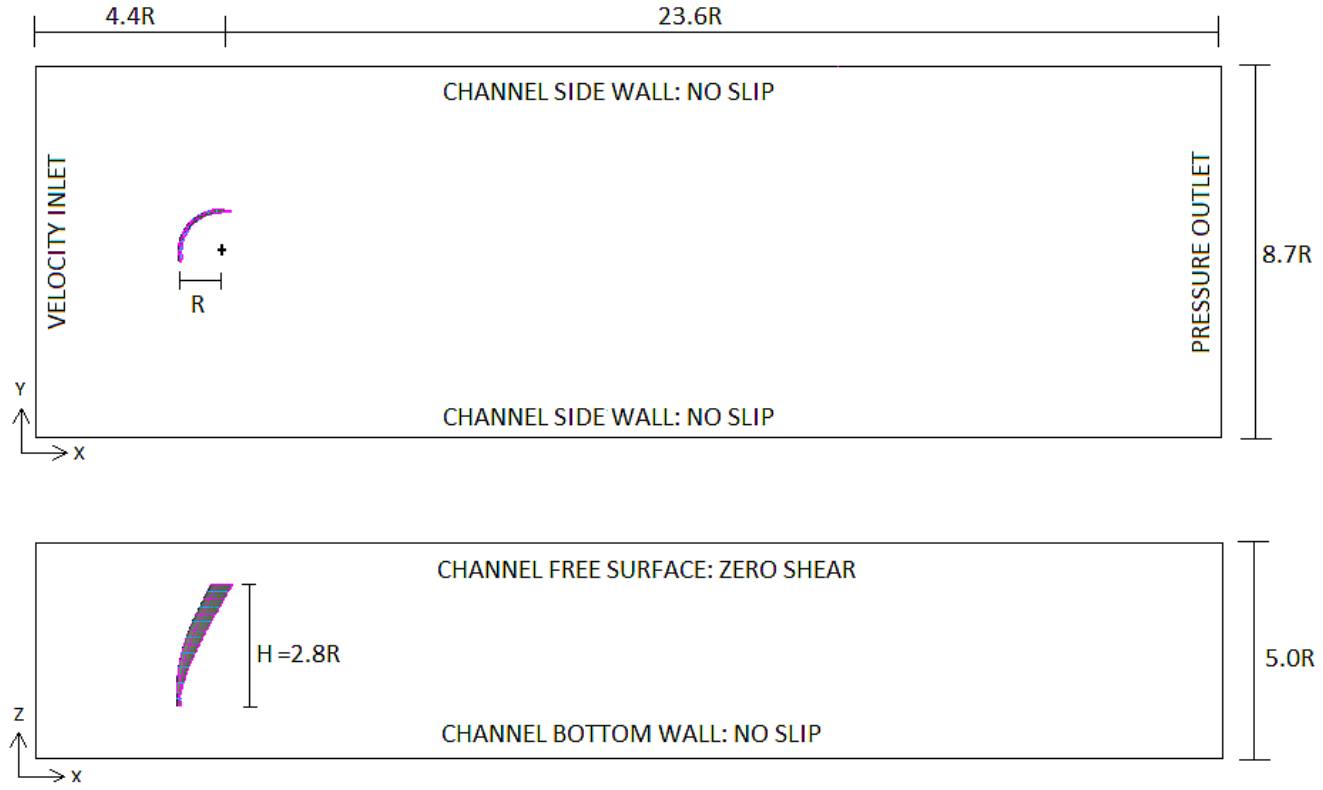

Figure 3.5: Top and side views of channel domain.

potential energy in a fluid flow, is low at 0.34. The Froude number is defined as

$$Fr = \frac{V_\infty}{\sqrt[2]{gh_\infty}} \tag{3.7}$$

with $V\infty$ and $h\infty$ being the velocity and height of the inlet conditions respectively. It was also visually observed in the experiments that the drop in free surface height at the turbine was minimal, confirming this as an adequate assumption. A velocity inlet condition and a pressure outlet condition were specified. The inlet velocity was set to match the experiment, measured at $0.7m/s$ by an acoustic doppler velocimeter (ADV). This device also provided data to estimate the inlet turbulent intensity $I = \frac{u\prime}{U}$ as 1.6%.

As depicted in figure 3.6 the swept area of the turbine perpendicular to the flow

relative to the channel area can be characterized by the blockage ratio $= \frac{S_{ref}}{ChannelArea}$ where $S_{ref} = 2RH$.

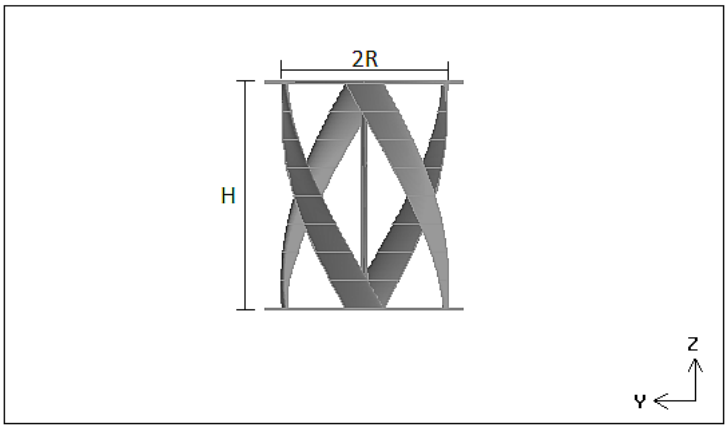

Figure 3.6: Visual representation of the 12% blockage ratio in the computational domain.

The modeled blockage ratio is kept consistent with the experiment at 12%. A large blockage ratio will result in an artificial channeling of the flow through the turbine, possibly leading to higher efficiencies than would be expected in an open tidal channel where the blockage ratio could be much lower. Efforts were made to minimize the blockage ratio in order to simulate free stream conditions in the experiment as much as possible. While 12% is a relatively small blockage ratio, it should be considered when using the results to estimate the behavior of a full scale turbine in a tidal channel as well as when comparing with other simulations or experiments.

3.6 Space Discretization

3.6.1 Single Static Blade

For modeling flow over a single static helical blade, an almost completely structured mesh was created as seen in figure 3.7. Structured meshes are preferred when possible

in order to limit excessive numerical diffusion.

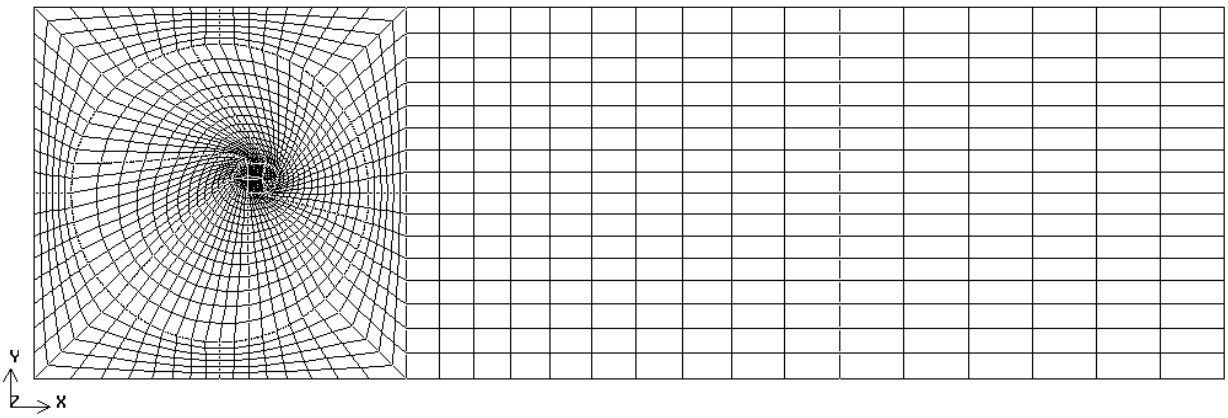

Figure 3.7: Mesh in xy plane for a single static blade.

The trailing tip of the blade has very high curvature and can lead to extremely skewed elements. The helical shape of the blade creates an unrecoverable level of skewness, exacerbating the problem at the blade trailing tip. Surrounding the blade, an oval mesh is used with an unstructured mesh at the trailing tip. For modeling using the wall function approach, the normal distance of the cell immediate to the blade wall, referred to as the first length, is set at 0.15 chords. This size was found to meet the requirement for the wall function modeling approach of $30 < y^+ < 300$. Because we are operating at a fairly low Reynolds number, this leads to a relatively large ratio of the first length to the chord length, indicating that the wall function modeling approach may give poor results.

When using the near-wall modeling approach, the mesh at the wall must be much more refined to meet the requirement of $y^+ \sim 1$. A first length value of 0.0001 chords is set to meet this requirement. The rest of the mesh domain must be resized accordingly to keep a moderate growth rate away from the blade. Refining in three dimensions increases the number of volume elements in the mesh by a factor of 2×10^4.

The contrasting mesh sections at the blade wall for the wall function approach and the near-wall modeling approach are presented in figure 3.8.

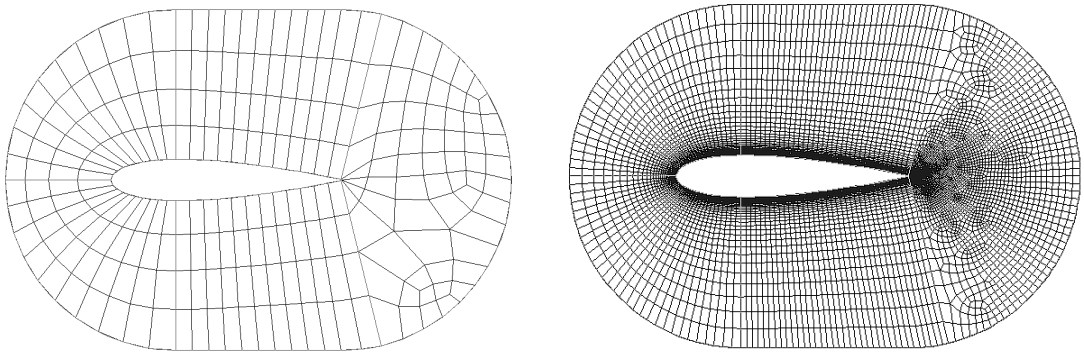

(a) Wall function modeling approach (b) Near wall modeling approach

Figure 3.8: Oval mesh for modeling in the near wall region

Determining the static torque values from flow over a blade stationed at various azimuthal positions was of interest, requiring a new mesh for each azimuthal location. The mesh was designed to be able to rotate the volumes of the inner cylinder containing the blade into the desired position, without needing to recreate the most detailed parts of the mesh. After the cylinder was rotated to the new location, the volumes connecting the cylinder to the channel walls were the only re-meshing needed. For the static configuration, it was assumed that the turbine shaft and end plates affected the flow minimally and were not modeled.

3.6.2 Four static blades

When modeling four stationary blades, it is no longer possible to keep a structured mesh in the area between the blades. A structured C-mesh around the blade and an unstructured grid surrounding this C-mesh is now used as scene in figure 3.9. A cooper-algorithm is used to sweep the mesh node pattern of these specified "source" faces along the helical edge of the blades.

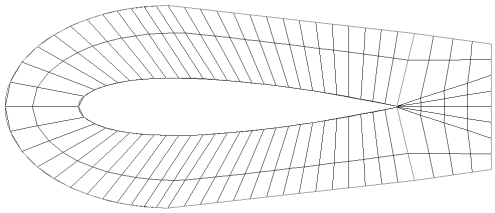

(a) C-mesh for wall function modeling

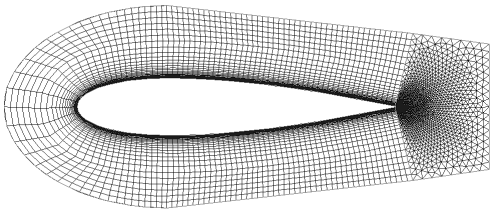

(b) C-mesh for near-wall modeling

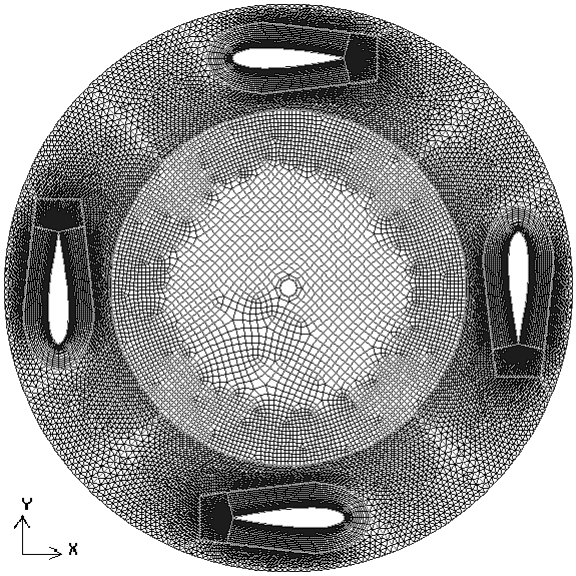

(c) Unstructured mesh connecting four blades

Figure 3.9: C-mesh for modeling in the nea- wall region

For both the stationary four-blade simulations as well as all of the rotating (both one blade and four blades) simulations, the turbine end plates and central shaft are included in the model as scene in figure 3.10.

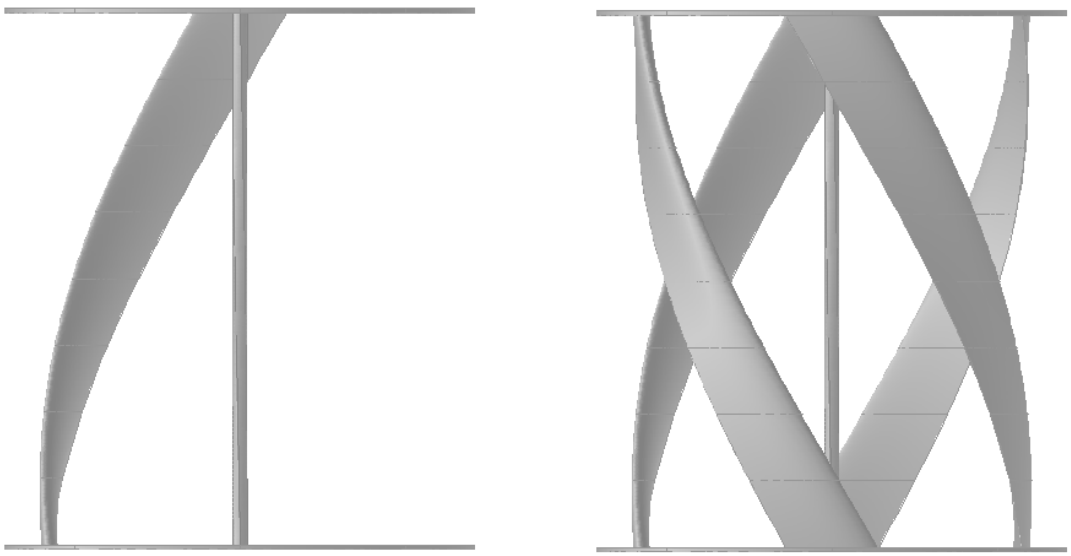

Figure 3.10: Full turbine configuration with end plates and central shaft.

3.6.3 Rotating Turbine

For modeling the rotating turbine with the sliding mesh technique, a rotating cylinder sub-domain was created that extends 1.2R from the turbine axis and matches the height of the turbine, capped by the two end plates. Figure 3.11 shows the interface surface for the rotating domain and the stationary domain, which were created with matching sized mesh grids to limit the numerical error in the transport across the interface.

3.7 Evaluation Parameters

The commercial computational fluid dynamics software ANSYS FLUENT v12.0 was used for the simulations. The software solves the flow governing equations using

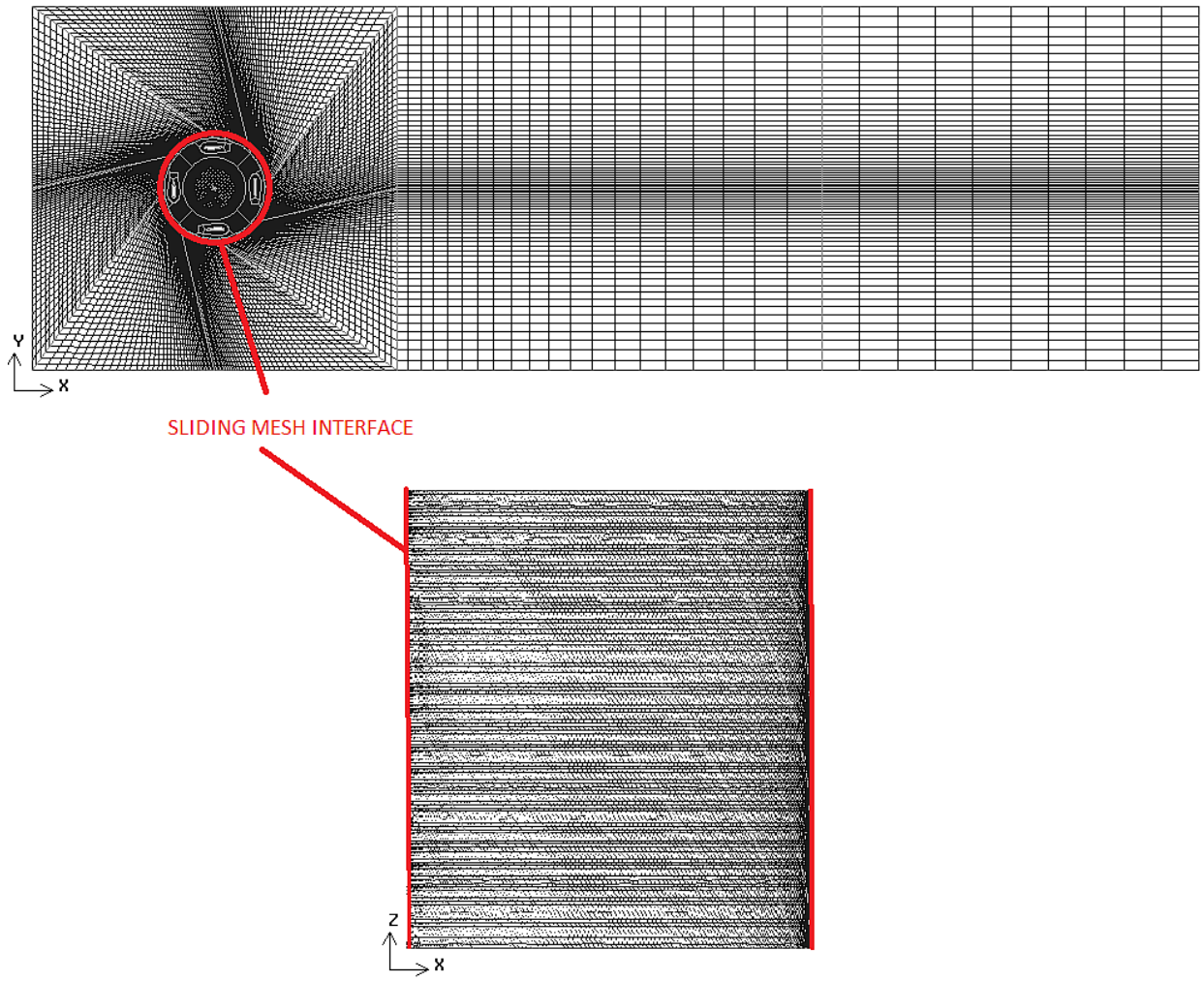

Figure 3.11: Sliding mesh interface

a cell-centered control-volume space discretization method. A pressure-based time-transient solver with absolute velocity formation was implemented in addition to the setings in table 3.1.

For the time discretization, it was found that a time step of 0.5 seconds was adequate for the static torque cases. For the rotating turbine simulations, a time step size that designated a 1.2 degree rotation per time step was sufficient to capture the flux across the the stationary-rotating domain interface and resolve the flow through the turbine.

Table 3.1: Fluent Settings and Solution Methods

Turbulent Model	Shear Stress Transport kω
Pressure-Velocity Coupling	SIMPLE
Discretization of Gradient	Green-Gauss Node Based
Discretization of Pressure	Second Order
Discretization of Momentum	Second Order Upwind
Discretization of Turbulent Kinetic Energy	Second Order Upwind
Discretization of Specific Dissipation Rate	Second Order Upwind
Transient Formulation	Second Order Implicit
Pressure Under-relaxation Factor	0.2
Momentum Under-relaxation Factor	0.6
Modified Turbulent Viscosity Under-relaxation Factor	0.6

Chapter 4

STATIC TORQUE ANALYSIS

4.1 Experiment Setup

Over the entire thesis I have used a set of experimental results that were carried out by Adam Niblick at the University of Washington's NNMREC as part of his M.Sc. Thesis for validation of the results presented here and for comparison to gain insight into the flow physics and numerical simulation strengths and challenge. The experiments were run for static ($\lambda = 0$) and dynamic configurations ($\lambda = 1.3,\ 1.6,\ 2.0,\ 3.2,\ 3.6$), and with the turbine in partial (single-blade) and full (four-bladed) configurations. A particle brake held the turbine at a stationary azimuthal position, while a reaction torque sensor recorded the static torque measurement. This was then repeated with the turbine located at various azimuthal positions. The free stream velocity was $0.7\ m/s$ and the Reynolds number was $Re_c = 28,000$ for all experimental results used for comparison and validation in this thesis. Additional information about the experimental setup is described in Niblick's Master's Thesis *Experimental and Analytical Study of Helical Cross-flow Turbines for a Tidal Micropower Generation System*[16]. Each helical blade spans a 90° range of azimuthal positions. For the description of the results, a single-bladed turbine's azimuthal position, θ, is described by where the top section of the blade is located. The bottom of the helical blade is located at $\theta + 90°$. For example, a blade indicated by an azimuthal position of $\theta = 45°$ has its top section of the blade at 45° and its bottom section at 135°. For the four-bladed static turbine, the azimuthal position is designated by the position of the blade's top section that is located in the quadrant of $0° \leq \theta < 90°$.

4.2 Single Blade Simulations

CFD simulations were performed for a single-blade configuration of the turbine. In each simulation, the blade was positioned at an angle, θ, with respect to the reference $\theta = 0°$ where the chord of the top airfoil is facing into the incoming current. Unsteady simulations were run until the values of reference physical properties reached a quasi-steady value, when the initial transient was washed away from the turbine and the flow, while unsteady, converged to the expected periodic behavior in the mean fluid variables, associated with the cyclic shedding of vorticity from the blade. This process was repeated 16 times, shifting the angular position of the blade by 22.5° and yielding results for the blade spanning the entire 360° range of possible positions. The static torque values from the CFD numerical model, as well as from the experiment, are shown in figure 4.1. In the static position, angles of attack range the full $-180° \leq \alpha \leq 180°$ meaning that the static torque is largely dominated by drag forces. There is very good agreement between the experiment and numerical results for blade positions of approximately $50° \leq \theta < 240°$. At the other azimuthal positions the numerical simulation results follow the same trend as the experiment, but there is a fairly significant over-prediction in the torque.

The helical blade spans 90°, which makes it is difficult to pinpoint what range of angles of attack create simulation difficulties leading to over-prediction in the torque. Paradoxically, there is good agreement for all positions where $|\alpha| > 45$ for the entire blade. The over-prediction of blade performance has been documented on numerous occasions for CFD numerical simulations using the Reynolds Average Navier Stokes (RANS) equations: the RANS equations are inherently incapable of accurately predicting the location of separation of flow in the boundary layer due to a smooth negative pressure gradient, and, therefore, the stall behavior for an airfoil or hydrofoil [25, 28, 29]. The separation which causes stall is typically predicted to occur at a larger angle of attack in the CFD simulations than is observed in experiments. This

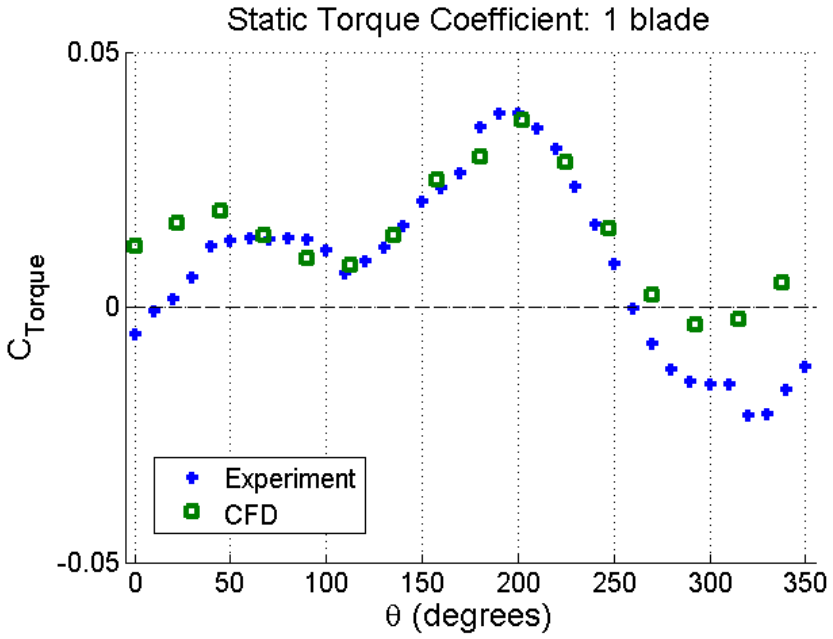

Figure 4.1: Coefficient of torque for a single static blade

leads to an over-prediction in lift and an under-prediction in drag, meaning an overall over-prediction in the torque, as seen in the presented numerical results. Depending on the airfoil geometry and Reynolds number, stall typically occurs for angles of attack in the $\alpha = 15°$ range. The location along the blade's chord length where separation occurs and the length of the separation region dramatically affects the lift and drag characteristics. The difficulty for RANS equations to predict this separation is especially marked at low-Reynolds number operating regimes where the transition from laminar to turbulent flow strongly influences performance [41–43].

Because the blades span 90°, it is difficult to tell exactly what range of α causes the divergence from the experimental results, but we hypothesize the following: at the low angles of attack such as figure 4.2(a) where the flow is fully attached ($-12° \leq \theta \leq 12°$), the simulation accurately predicts the flow. As the angle of attack increases into the stall regime as in figure 4.2(b), the RANS equations cannot predict the precise

separation location along the blade wall, creating the discrepancy in the quantitative prediction of the torque, while still predicting the right trend. For a static blade, it can be positioned so the flow is actually coming in perpendicular or even at the tail section as shown in 4.2(c) and 4.2(d). At these very high angles of attack, the blade geometry imposes very sudden negative pressure gradients and the location of separation can be accurately predicted once again. This explains why we see very good agreement when the angle of attack for all sections of the blade is greater than 45°. It is somewhat counter intuitive that we see the large discrepancy in the results at blade positions centered around the very low angles of attack, where we expect the best agreement; however, these low angles of attack are a small region, with large regions of stall on either side. When the blade goes through the region with low α, because the blade spans 90°, a large portion of the blade is still in the stall region.

In an effort to improve the static torque simulation results, the modeling in the near-wall region was investigated. As described in further detail in Chapter 3, the modeling in the near-wall region can be done using the wall function approach or the near-wall modeling approach. The wall function approach was applied for the simulations presented in figure 4.1. In the wall function approach, the sub-viscous layer is not resolved and semi-empirical equations are instead used to model the flow in this near-wall region. Alternatively, the near-wall modeling approach can be applied in which the sub-viscous layer is fully resolved, requiring a much higher level of element refinement. A refinement of the mesh for the static blade to use the near-wall modeling approach led to approximately a 20 times increase in computation time.

The plot of static torque results including the near-wall modeling simulations can be seen in figure 4.3. The near-wall modeling approach shows very good agreement, similar to the wall-function approach, for a large range of blade positions, $50° \leq \theta \leq 240°$. In the region where there is disagreement between the CFD and experiment we see a 20-25% reduction in the error using the near-wall modeling approach. This error could likely be reduced further by additional refinement in the near-wall mesh

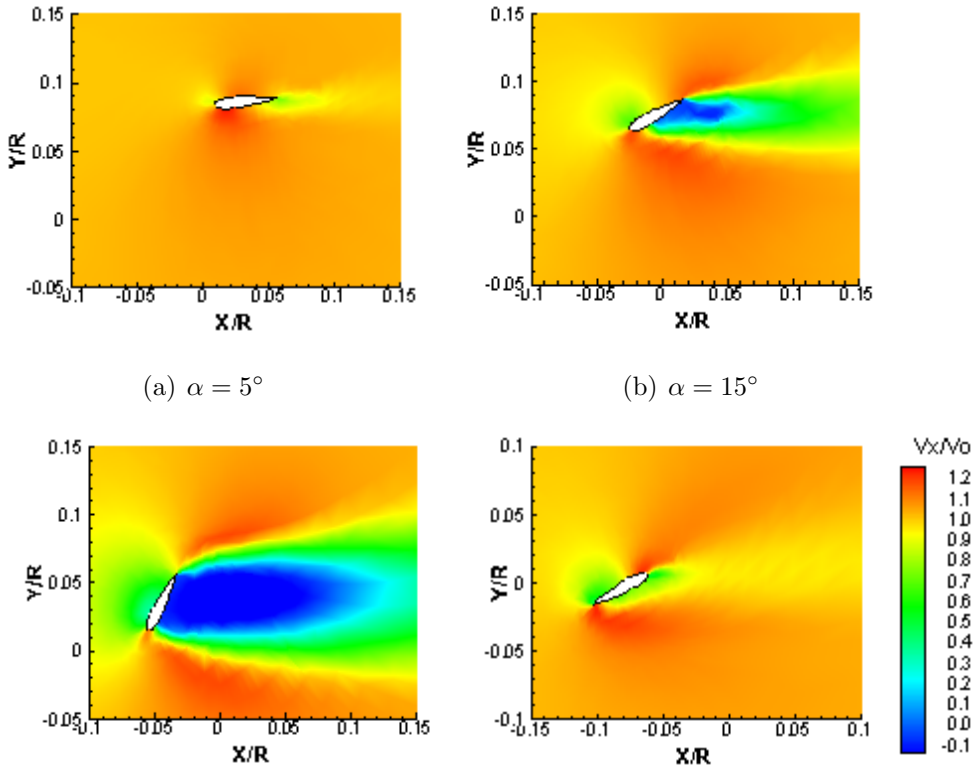

(a) $\alpha = 5°$ (b) $\alpha = 15°$

(c) $\alpha = 65°$ (d) $\alpha = 205°$

Figure 4.2: Velocity contour plots of static blade for various angle of attacks: flow coming from left

such as including more nodes along the blade profile, but this may only improve the results slightly with much greater computational cost.

4.3 Four Blade Simulations

The structure of the domain mesh had to be altered slightly to be able to accommodate four blades as described in Chapter 3. It was verified that this alteration of the mesh produced the same simulations results for a single blade as the original single-bladed mesh used for the results presented above.

For the four-bladed turbine, the blades are distributed evenly around the circumfer-

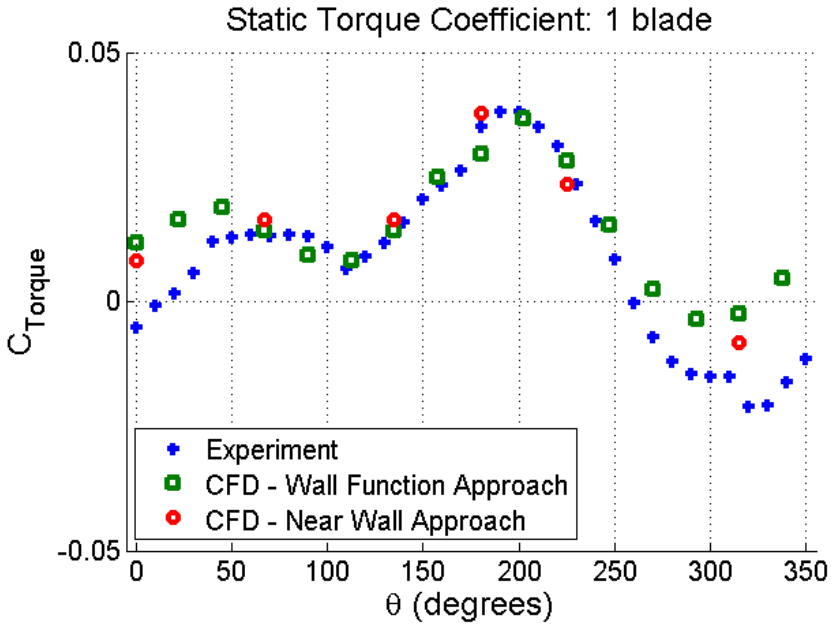

Figure 4.3: Coefficient of torque for a single static blade including near wall modeling

ence of the cylinder, suggesting that there be an approximately constant total turbine static torque for the various azimuthal positions. Both the experiment and numerical results, as presented in figure 4.4, do indeed show an almost constant torque value, compared to the range of variations observed in the single blade results presented in figure 4.1. Variations from the constant value can be explained by the effect of the wake shedding from one blade on another blade downstream. Notice that the plot has azimuthal positions of $0° \leq \theta < 90°$ because for the four-bladed turbine the configuration repeats itself every 90°. The four-bladed turbine again shows a slightly higher simulated torque than the experiment torque due to the same effects discussed for the single blade case.

The experiment shows a very large drop around $\theta = 70°$. The large drop can be explained by a large wake effect occurring for this azimuthal position where the bottom half of the front blades occupy the angular ranges from 25° to 70° and 115° to

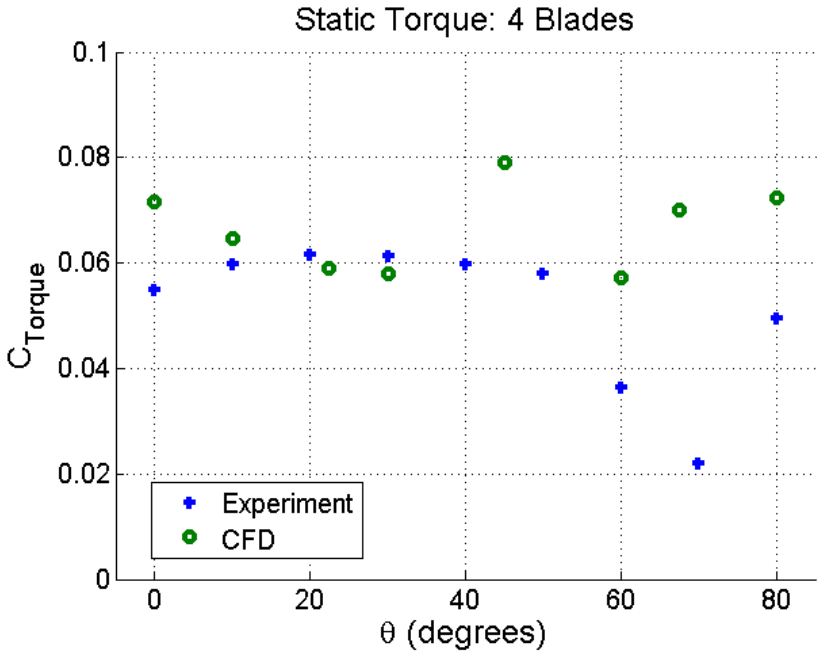

Figure 4.4: Coefficient of torque for a static four-bladed turbine

160°, directly in front of the bottom half of the back blades (which sit at 290° to 335° and 200° to 245° respectively). It is likely that in the CFD simulation there is numerical error that diffuses the wake more quickly than in the experiment, meaning that the simulation cannot capture this wake-blade interaction and, therefore, misses the resulting large drop in static torque.

It is also interesting to compare the results from the four-bladed static turbine to the single-bladed turbine. Figures 4.5 and 4.6(a) show these results for the experiments and simulations respectively. The plots show the static torque values for the four-bladed turbine compared to the summation of torque values from the single blades that are located in the same positions as the blades in the four-bladed turbine. In both the experiment and the simulation, there is a higher overall static torque in the full turbine configuration than in the composition of four single-bladed results. We hypothesize that the increase in solidity, and therefor the effectibe blockage ratio,

associated with the four-bladed turbine, compared to the single blade configuration, alters the flow field slightly, resulting in a small increase in static torque for each individual blade and improved performance at zero tip speed ratio. We achieve a more detailed comparison in figure 4.6(b), which contains the same information as figure 4.6(a), but is presented on an individual blade basis. For example, the values from $\theta = 0°, 90°, 180°$, and $270°$ in figure 4.6(b) sum to the value at $\theta = 0°$ in figure 4.6(a). A large difference in torque values, such as the decrease in torque at $200°$, between the single blade and four blade values indicates strong wake effects. Despite these wake effects that will tend to reduce performance, there is a general trend of a small increase in predicted torque at the four-bladed turbine simulation compared to the single blade simulation, for almost all azimuthal positions, consistent with the global positive effect of high blockage and solidity ratio, over the point-wise effect of wakes.

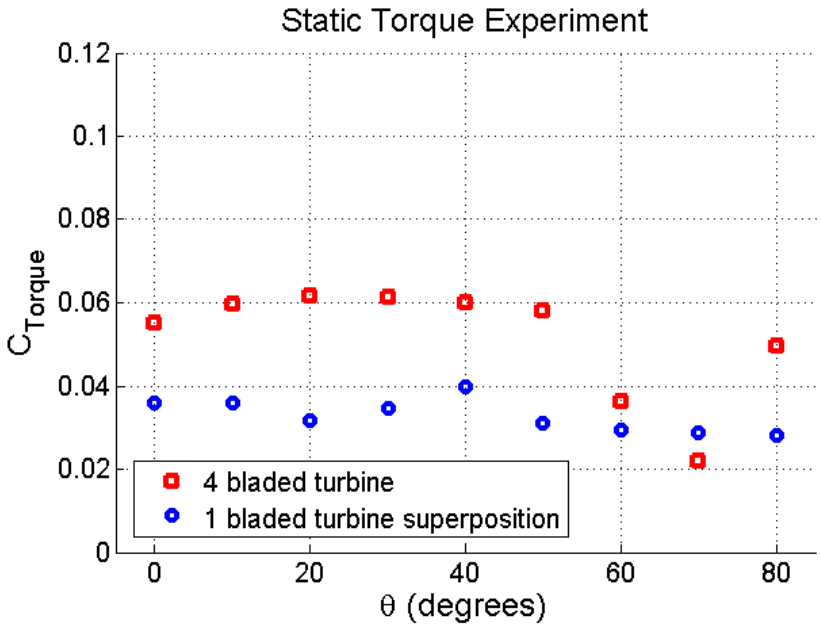

Figure 4.5: Static Torque Experiments - four-bladed turbine vs. superposition of single blades

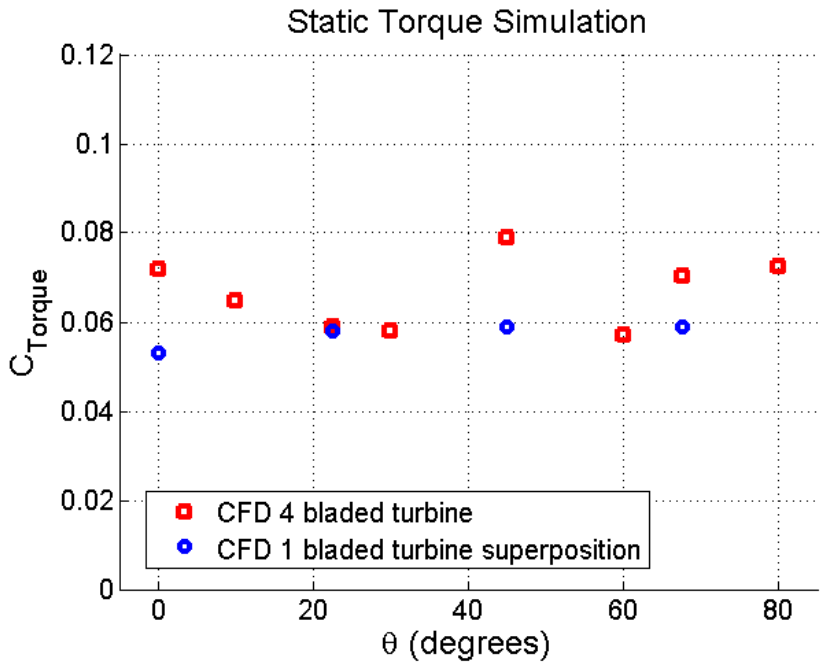

(a) CFD- four-bladed turbine vs. superposition of single blades

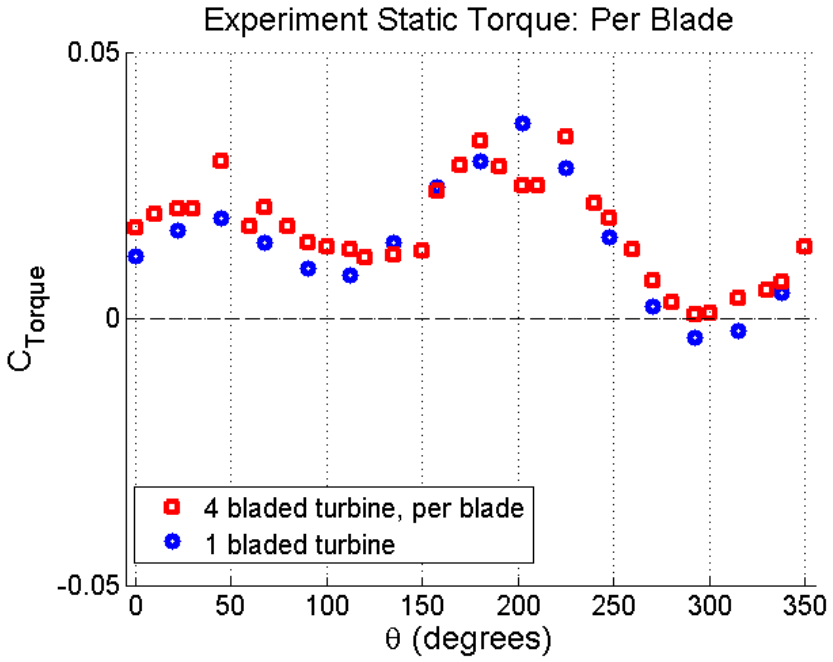

(b) CFD- four-bladed turbine individual blade torque vs. torque of single blade

Figure 4.6: CFD static torque

Chapter 5

ROTATING TURBINE: DYNAMIC TORQUE ANALYSIS

The sliding mesh technique described in Chapter 3 was used to simulate the turbine under operating conditions. Five operating conditions were tested, at tip-speed ratios of 1.3, 1.6, 2.0, 3.2 and 3.6. Both the single-blade configuration and the full four-bladed turbine were simulated to provide insights into the physics of the flow around the turbine blades. Comparison from experiments conducted by Adam Niblick for his thesis at the UW [16] are presented for validation, comparison and analysis.

5.1 Single-Bladed Rotating Turbine

5.1.1 Mesh Convergence Study

A mesh convergence study was performed for a single-bladed turbine operation at a tip speed ratio of $\lambda = 3.2$. The three grids studied are described in table 5.1. The hydrodynamic torque for each simulation is presented in figure 5.1. The first grid has the lowest level of refinement and is designed to use the wall functions, which are described in Chapter 3. Unlike a static blade, a rotating blade sees large and rapid changes in angle of attack. This means the empirical equations used in the wall function modeling approach may have more difficulty resolving the flow within the boundary layer for the dynamic case. The inadequacy of the wall functions for the rotating turbine is clearly evident from the prediction of a negative average turbine torque by the simulation using wall functions and a coarse grid.

It is apparent from the failure of the wall-function modeling approach in this rotating application that the viscous sublayer must be resolved to accurately simulate the flow at the moving wall. The second grid has a higher level of refinement, necessary

Table 5.1: Mesh-Grids for a Single Rotating Blade

Mesh	Refinement	Wall modeling	Total Elements	First Node from Wall (mm)	Nodes on Blade Profile
1	coarse	wall functions	531,896	6	56
2	medium	near-wall	4,602,498	0.004	148
3	fine	near-wall	7,789,954	0.001	252

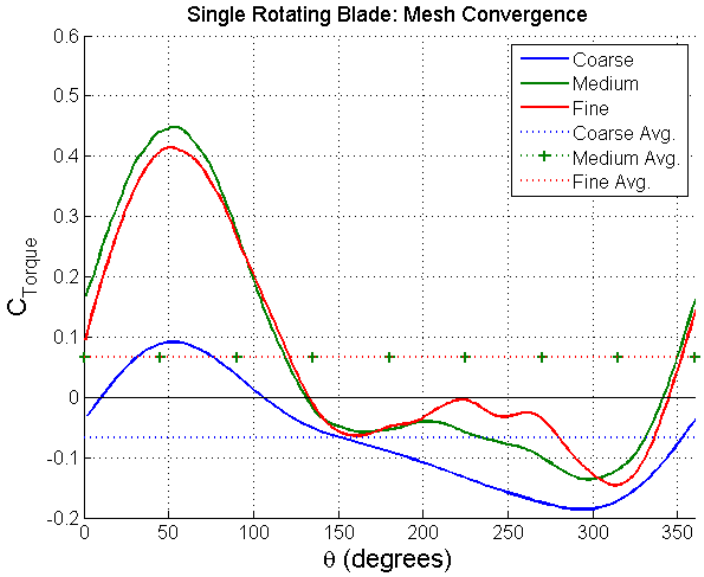

Figure 5.1: Plot of dynamic torque results for mesh-grids of different refinement levels for $\lambda = 3.2$

to capture the boundary layer dynamics directly through the near wall modeling approach. The third grid is refined further near the blade walls, in order to produce a more accurate representation of the boundary layer flow at this value of the Reynolds number. The results from the simulations using the second and third grids present some slight variations in the instantaneous torque but give predictions of almost

exactly the same average torque. We determined that the intermediate refinement in the grid (our medium grid) was the optimum trade off in precision and computational cost, providing sufficient resolution inside the boundary layer to capture its dynamics accurately while keeping the computational run time and memory requirements within reasonable limits.

5.1.2 Numerical Simulations of the Rotating Turbine using the Sliding Mesh Technique

Numerical simulations for a single-bladed rotating turbine were performed for three tip speed ratios: $\lambda = 1.6$, $\lambda = 3.2$, and $\lambda = 3.6$. Figure 5.2 shows the plot of the hydrodynamic torque for each case as a function of position. While experiments at $\lambda = 1.6$ were not achievable in the experimental setup tested, this value of the tip speed ratio is characteristic for the high solidity four-bladed turbine and therefore the analysis of the single-bladed case at this operating condition allows for direct comparison of these two configurations. This comparison gives us a window into the physics of the flow in high solidity operation and in blade-wake interactions. Each case's average hydrodynamic torque is given in table 5.2. In the experiments, $\lambda = 3.2$ had the highest attainable particle brake torque value and, as expected, $\lambda = 3.2$ has the highest average torque for the simulated cases.

Table 5.2: Simulation Torque Averages for the Single Rotating Blade

λ	$C_{avg\,Torque}$
1.6	0.047
3.2	0.065
3.6	0.057

For tip-speed ratios 3.2 and 3.6, the peaks for the torque curves should occur when the angle of attack reaches its maximum pre-stall angle, which for a 2-D blade element

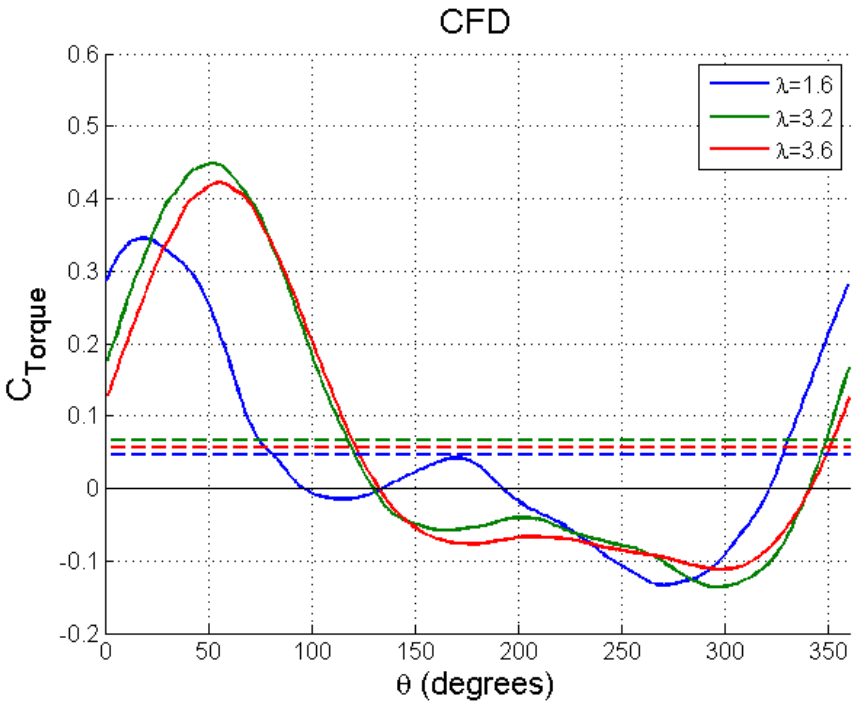

Figure 5.2: Plots of coefficient of torque for numerical simulations for a single rotating blade

is near $\theta = 90°$ and $\theta = 270°$. In each simulation case we see a peak value when the blade's top section azimuthal position is approximately 45° and a smaller peak at approximately 235°. These positions correspond to when the blade is centered about $\theta = 90°$ and $\theta = 270°$ respectively. For $\lambda = 1.6$, the stall angle of attack is reached at a lower θ as previously shown in figure 1.8, which explains why the torque peak location is shifted to a lower azimuthal position. The second peak in each case is lower due to velocity deficit and wake effects from the upstream side of the turbine rotation.

5.1.3 Model Validation

Experiment Setup

The experimental setup for the dynamic torque measurements on the rotating turbine was very similar to that of the static case. A particle brake was used to apply a resistive torque on the turbine shaft, controlling the rotational speed of the turbine. Setting the particle brake to various levels of resistance torque allows for turbine operation at different tip speed ratios. The reaction torque sensor measures the torque that the particle brake applies on the turbine. The reading also includes some residual torque resistance applied from the optical encoder, which is set to record either the rotational velocity or the azimuthal position. The particle brake resistance is set, and then the turbine is allowed to start up rotation. Once the rotation has reached a statistical steady state, the measurements of the dynamic torque are recorded. As in the case of the static turbine simulations and experiments, the free stream velocity was set at $0.7\frac{m}{s}$ for all cases.

In order to provide measurements at the highest value of tip speed ratio for this turbine in this configuration, we set the particle brake to an unloaded position. In this operating condition, we measure the dynamic behavior of the turbine under no external load, as it essentially spins freely. The reaction torque sensor still measured very low levels of torque in this case, due to the residual torque at the shaft from the inherent resistance from the particle brake and optical encoder. There was an additional residual component of resistance torque applied on the shaft by the bearing and the fixed point that held the shaft in place that was not quantified in the experiments.

For single blade experiments, it was very easy for the turbine to stall due to the large oscillations in the hydrodynamic torque produced by the blade as it traverses the circumferential trajectory and the lack of inertia necessary to pass through the locations where the hydrodynamic torque is negative. This resulted in a very limited

range of stable operational tip speed ratios. Experimental results under load were obtained for $\lambda_{avg} = 3.2$, which was the slowest attainable mean rotational speed before stall occurred. The single rotating blade experiment was also performed for a free spinning case where the particle brake was unloaded. The free spinning resulted in a tip speed ratio of $\lambda_{avg} = 3.6$. For the four-bladed rotating turbine, there was a much larger range of stable operational tip speed ratios. Experimental results were attained for tip speed ratios in the range of $\lambda = 1.3$ to $\lambda = 2.2$.

System Dynamics

For the experiment of the single rotating blade, the angular acceleration over the period of the turbine's rotation is significant, meaning some model of the turbine as a dynamical system is necessary to interpret the results from the experiments and enable them to be compared with the simulations. Figure 5.3 gives a free body diagram for the system. The forces exerted by the fluid on the blades create the hydrodynamic torque, driving the turbine's rotation. There is also a frictional torque countering this which includes the friction in the turbine bearings as well as drag induced from other rotating parts of the turbine. Also countering the rotation, is the torque applied from the particle brake, given by the measurement from the reaction torque sensor. The sum of all of these torque moments is equal to the moment of inertia multiplied by the angular acceleration. The resulting dynamic balance equation is given by:

$$I\frac{d\omega}{dt} = \sum M_{ext} = T_{Hydrodynamic} - T_{ParticleBrake} - T_{SystemFriction} \tag{5.1}$$

In the static torque case, the system is much simpler; the angular acceleration is zero, and there is essentially no system friction, meaning the hydrodynamic torque is very approximately equal to the particle brake torque. The CFD simulation models the hydrodynamic torque, and the reaction torque sensor gives the particle brake torque, therefore a direct comparison can be made between the experiment torque

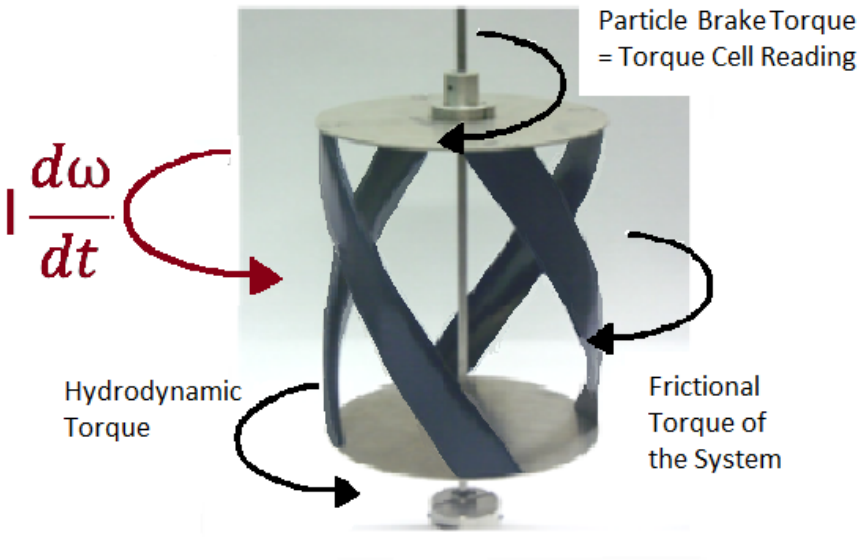

Figure 5.3: Free body diagram of dynamic torque system

cell measurement and the CFD analysis. For the rotating single-bladed turbine, this is not the case.

We analyze the measurements collected from the optical encoder for the experiments with the rotating single blade turbine. The optical encoder recorded angular position as a function of time and, from this data, the angular velocity was calculated. The data from the optical encoder was digitized and recorded at a relatively low sampling rate (20 Hz). For the case of $\lambda_{avg} = 3.2$, this meant the "instantaneous" angular velocity was calculated as an average over about 70°. The calculated angular velocity from the experimental measurements, shown in figure 5.4, paint a picture in which the large oscillations of hydrodynamic torque combines with the low inertia of the single blade turbine to produce a significant variation in the angular velocity over each cycle. Again, because of the low sampling rate, the experimental data is not differentiable in time and can only be interpreted in a phase averaged sense, as presented in the figure 5.4. Taking advantage of the periodicity of the system, a Fourier transform is applied

to the data in order to determine a best functional representation of the angular velocity as a function of azimuthal position. This function can now be differentiated to calculate the angular acceleration and model the dynamics of the turbine according to equation 5.1. The result of this differentiation is plotted in 5.5.

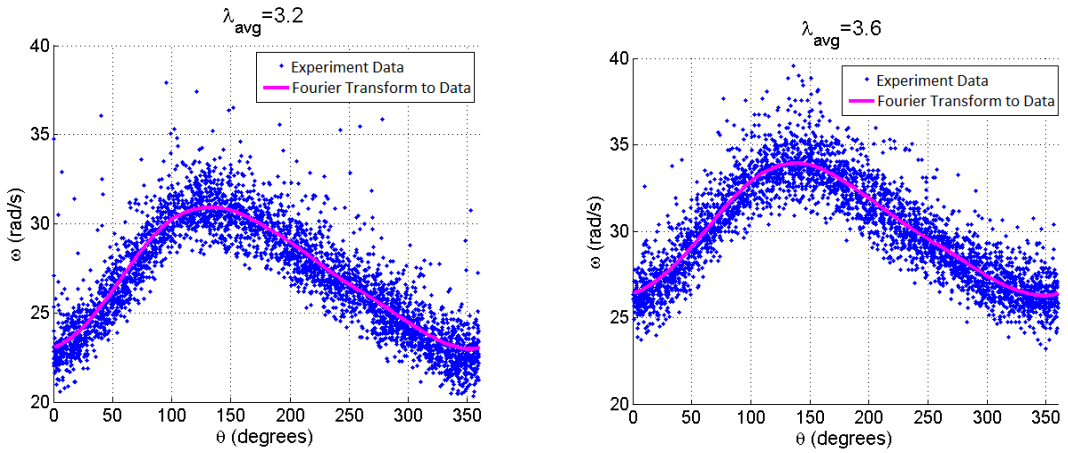

(a) λ=3.2 (b) λ=3.6

Figure 5.4: Plot of angular velocity in the single rotating blade experiment

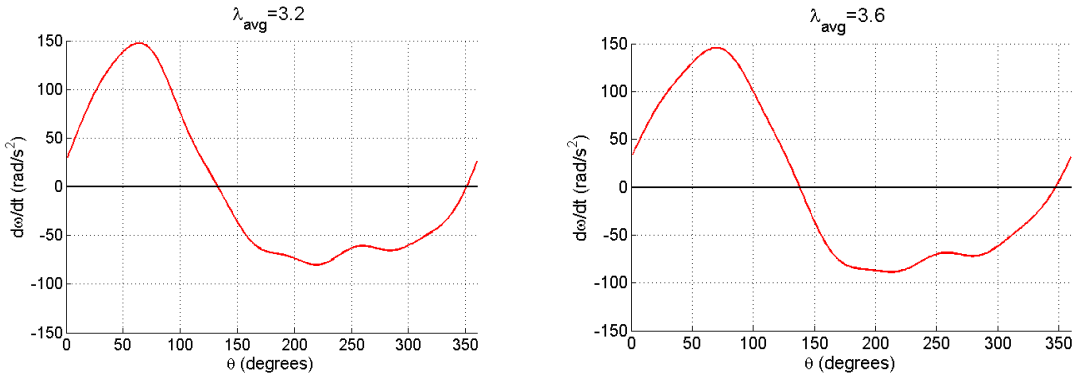

(a) λ=3.2 (b) λ=3.6

Figure 5.5: Plot of angular acceleration in the single rotating blade experiment

The moment of inertia of the turbine is calculated from the CAD design and the use

of a few simplifying assumptions for the auxiliary items needed for the experimental mounting of the turbine in the water channel. The blade and the end plates of the turbine have the highest moments of inertia for the system. It is assumed the moment of inertia for the small rotating parts that are installed close to the axis of rotation, such as the turbine shaft and various bearings, can be neglected. SolidWorks is used to calculate the moment of inertia for one blade: $I_{blade} = 0.93 \times 10^{-3}\, kg\, m^2$. The moment of inertia for each end plate is calculated from the moment of inertia for a thin circular disk: $I_{plate} = \frac{3}{2} m R^2$ where m is the mass and R is the radius. This totaled to a moment of inertia for the system of $I = 1.9 \times 10^{-3}\, kg\, m^2$.

Once the moment of inertia and the angular acceleration are determined, these values can be used in equation 5.1 to compare the experimental measurements from the torque cell, which is almost constant, against the results from the CFD simulations, which show large variations of the instantaneous hydrodynamic torque produced by the flow on the turbine blades. When we add the inertial term calculated from differentiating the angular velocity and position data to the torque cell measurements, we obtain a value equal to the hydrodynamic torque minus the frictional torque. Assuming that the frictional torque is small compared to the other terms in the equation, this newly calculated value can then serve as a comparison to validate the CFD results. Figure 5.6 plots the torque raw measurements and the value of hydrodynamic torque calculated including the dynamics model (torque measured plus inertial term).

The system dynamics are periodic and therefore the integral of the inertia term (left hand side of eq. 5.1) over the cycle is identically zero (eq. 5.2). As a result, the average hydrodynamic torque over the period is equal to the sum of the average particle brake torque plus the average frictional torque, as shown in eq. 5.3.

$$\int_{0^\circ}^{360^\circ} I \frac{dw}{dt}\, d\theta = 0 \tag{5.2}$$

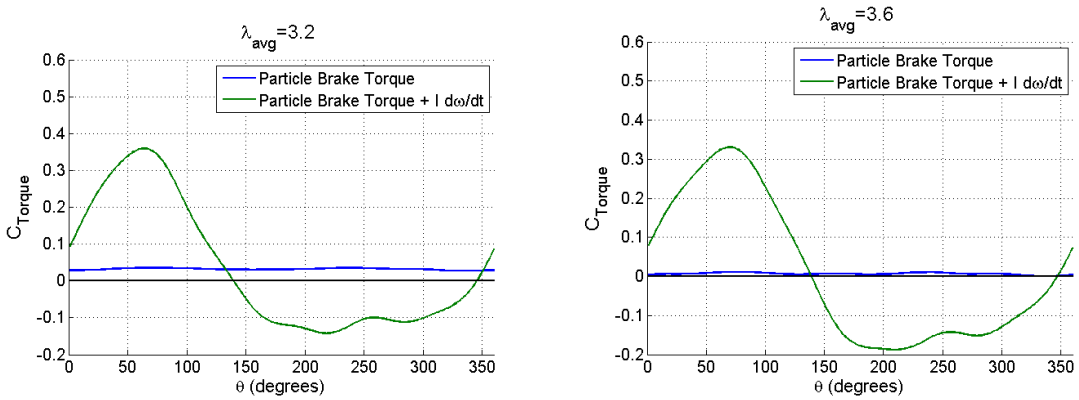

(a) λ=3.2 (b) λ=3.6

Figure 5.6: Plot of torque in the single rotating blade experiment

$$\overline{T_{Hydrodynamic}} = \overline{T_{ParticleBrake}} + \overline{T_{SystemFriction}} \tag{5.3}$$

For the case of a four-bladed turbine, the blades are distributed evenly, indicating that there should be a fairly constant hydrodynamic torque through the turbine's cycle. The inertia of the turbine is also significantly higher, up to 2.5 times higher. This means that there is very little angular acceleration. Therefore, the CFD results can be compared directly to the experiment torque measurements (assuming the frictional torque on the system is small).

Comparison of Simulations with Experimental Results with the Support of Dynamical Modeling

The experiment results for $\lambda_{avg} = 3.2$ and $\lambda_{avg} = 3.6$ can be used to validate the numerical model. Figure 5.7 shows the plots of the CFD simulation instantaneous torque values, compared to the combination of the torque cell measurements and the inertia term in equation 5.1. The average values within a cycle are shown. The raw torque data collected from the reaction toque cell is plotted and deviates only

very slightly from the average experiment torque. These plots clearly demonstrate the higher quality comparison between the numerical simulations and experiments created by including the calculated inertial term, rather than simply a direct comparison with the raw torque sensor data.

For both tip speed ratios, we observe an over-prediction by the CFD simulation of the average torque, but also appreciate very similar qualitative and quantitative features in the instantaneous torque curves. Differences in these curves can be attributed to the varying tip speed ratio in the experiment. Since the experiments found the peak average torque for this configuration at a tip speed ratio $\lambda_{avg} = 3.2$, our hypothesis is that when the turbine is operating at rotational speeds both higher and lower than that for $\lambda_{avg} = 3.2$, the turbine is producing lower torque than it would if operating at the constant tip speed ratio $\lambda = 3.2$, as modeled in the simulation. Thus, the varying rotational velocities, in addition to the frictional torque present in the experiment but not in the numerical model, contribute to the model's over-prediction of the average torque.

The numerical simulation models the turbine hydrodynamics at a constant tip speed that is matched to the average tip speed ratio of the experiments; however, because the experiments have a significantly varying tip speed ratio (as shown in figure 5.4, the direct comparison does not provide 100% quantitative agreement. Further analysis of the flow physics induced by the difference in operating conditions between the experiments and the simulations can provide deeper insight into the limits of the quantitative comparison of turbine performance. As the tip speed ratio changes, the angle of attack and relative Reynolds number changes significantly, directly impacting the lift and drag forces on the blade. When $\lambda_{avg} = 3.2$, the tip speed ratio has a range of $2.8 \leq \lambda_{avg} \leq 3.6$, and when $\lambda_{avg} = 3.6$, the tip speed ratio has a range of $3.2 \leq \lambda_{avg} \leq 3.8$. The varying Reynolds number and angle of attack for the different tip speed ratios can be seen in figure 5.8. At low-Reynolds numbers, even small changes in the Reynolds number can significantly affect the coefficients of lift and

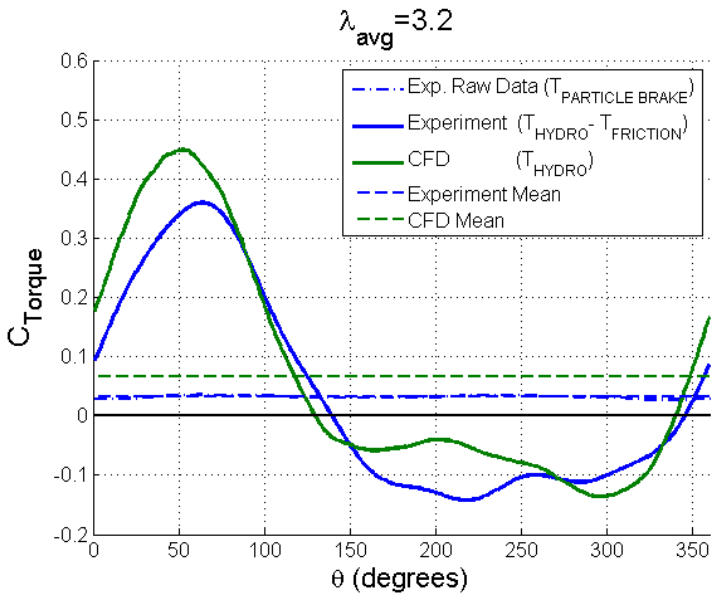

(a) λ=3.2

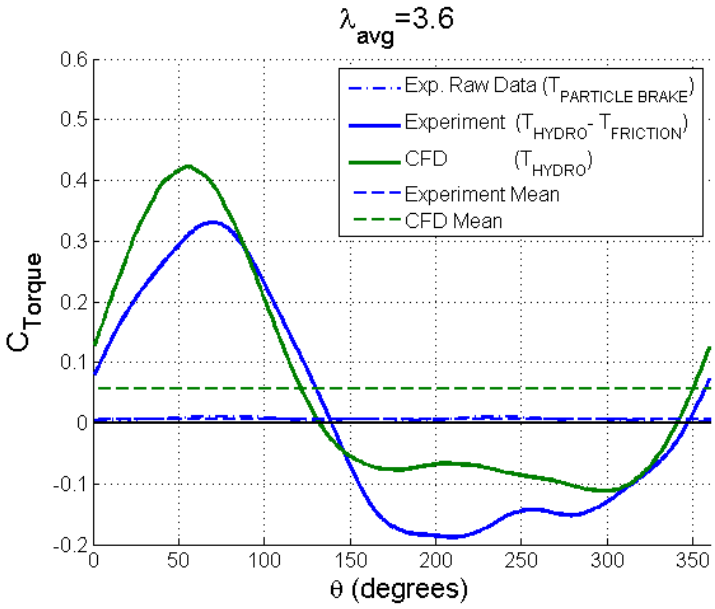

(b) λ=3.6

Figure 5.7: Plot of torque for a single rotating blade

drag. This is evident in figure 5.9 which provides data from experiments performed by Sandia National Laboratories for flow over a static straight bladed NACA 0018 airfoil [44]. At the same time, the turbine performance hits a maximum at a given tip-speed ratio given by the increased impedance to flow, even at higher Reynolds number. These two effects lead to slight differences in the data presented, highlighting the complexity of the cross flow turbine physics.

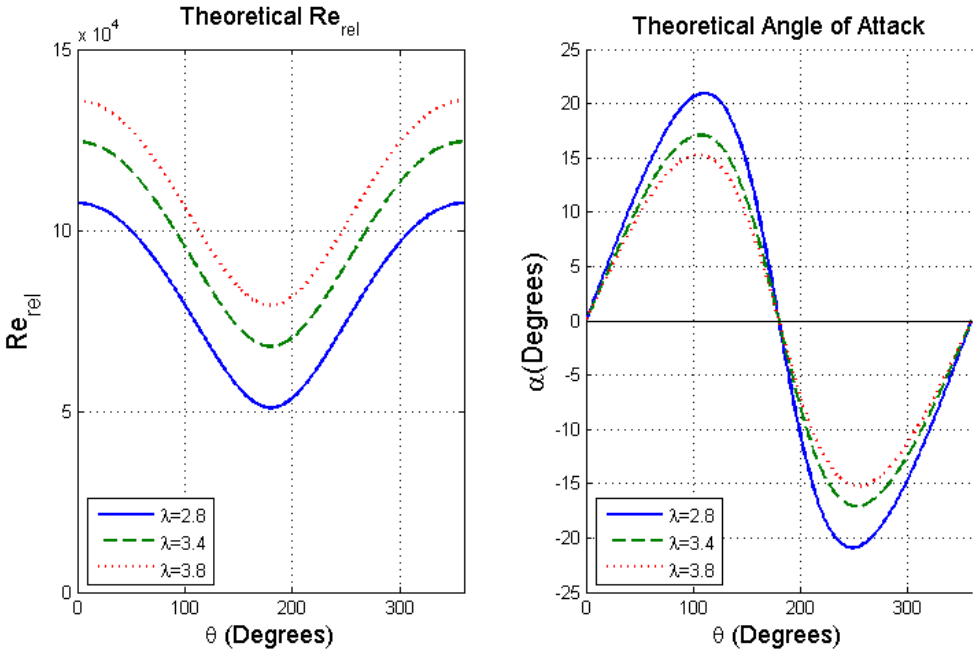

Figure 5.8: Theoretical Reynolds number and angle of attack for the tip speed ratios occurring for $\lambda_{avg} = 3.2$ and $\lambda_{avg} = 3.8$

The average torque values for the experiment and CFD model for a single rotating blade are summarized in table 5.3. The table shows a larger disparity between the experiment and CFD simulation for the larger tip speed ratio. This can be partially explained by the dependency of the residual friction torque that increases with increasing rotational velocity. In an effort to better characterize the torque as a function of the rotational velocity, the difference between the CFD and experiment torque

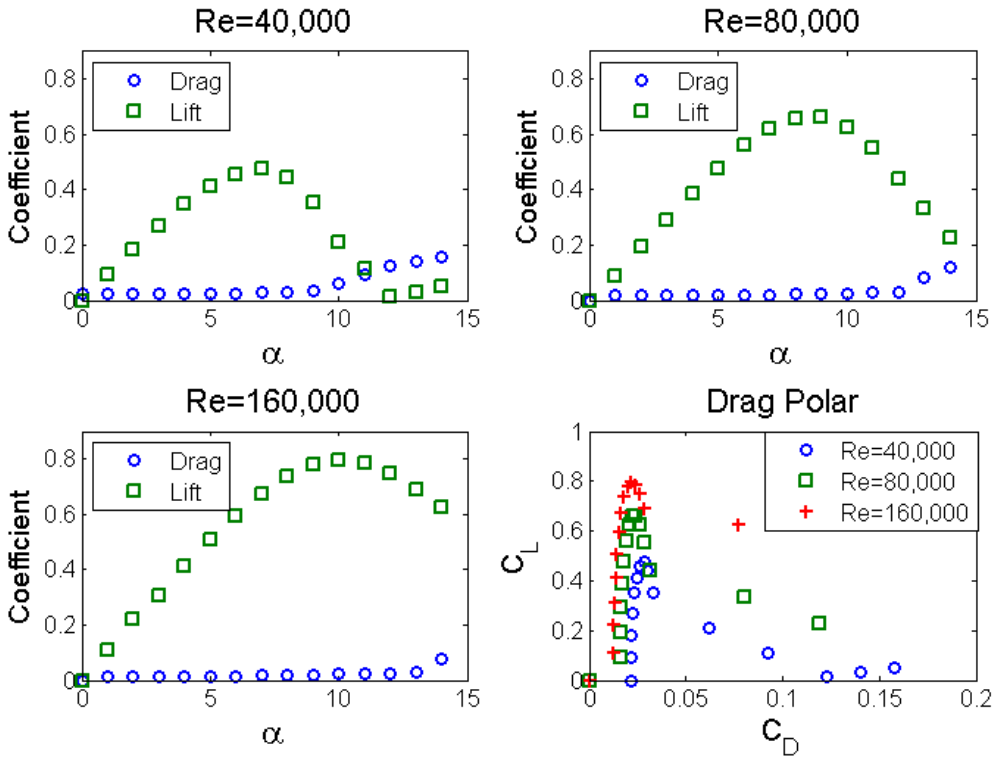

Figure 5.9: Drag and lift data for a NACA 0018 airfoil from Sandia National Laboratory experiments. Source [44]

curves were calculated. Figure 5.10 shows this difference for both data sets. There is no consistent dependency of the difference, taken as a model for the frictional torque, with the angular velocity. The difference between the two curves is likely largely dominated by the discrepancy between the hydrodynamics in the simulation at a constant tip speed ratio and that in the experiment where the blade was experiencing flow at varying tip speed ratios. The characterization of the residual friction torque by subtraction of the measured from the simulated torque is, therefore, difficult and results in uncertain values.

A better comparison could be made between the experiment and CFD model for a

Table 5.3: Average Coefficient of Torque for Single Rotating Blade

λ	Experiment	CFD
3.2	0.032	0.065
3.6	0.007	0.057

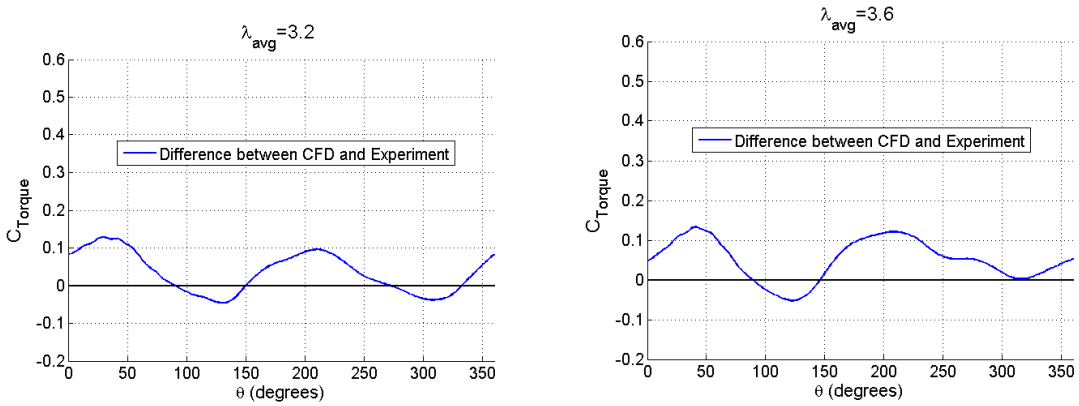

(a) λ=3.2 (b) λ=3.6

Figure 5.10: Plot of the difference between CFD and experiment instantaneous torque. This difference can be interpreted as an indication of the residual friction torque, which is a function of angular speed.

single rotating blade if simulations were run at the various angular velocities occurring in the experiment and a composite CFD torque curve was created. The best comparison could be achieved by performing the experiment using a device with a variable load to keep the turbine rotating at a constant speed. Fortunately, for a turbine with evenly distributed blades such as the four-bladed turbine, the hydrodynamic torque undergoes much smaller fluctuations throughout the cycle, and the moment of inertia is much higher (approximately 2.5 times larger) so the oscillations in the rotational velocity are very small. These features were confirmed from the experimental results and the comparison of CFD and measurements in the four-bladed turbine were not

influenced by this issue.

While the instantaneous values of hydrodynamic torque from the simulations and the experiments did not matched exactly, the simulation predicted accurately the qualitative trends observed in the experiments. The quantitative comparison of the torque values showed good agreement in both instantaneous and mean values over the cycle. The source of the discrepancies, namely the frictional torque and the unsteadiness in angular velocity, were identified and their order of magnitude estimated to provide a bound for the error. The similarities in the torque curves for the experiments and CFD simulations are evidence of validation that the presented sliding mesh RANS model can simulate, with reasonable accuracy, the hydrodynamic torque of a Cross Flow Hydrodynamic rotating turbine.

5.1.4 High Reynolds Number Simulation

The CFD simulations were computed for conditions that matched the laboratory testing parameters. The Reynolds number is much lower for the turbine in the lab than for the full scale micropower turbine, which is lower still than what would be experienced by a commercial scale turbine. A benefit of numerical simulation is that a large change in the Reynolds number can be achieved more easily than changing the Reynolds number for an experiment, which would involve manufacturing a much larger turbine and finding or building a much larger testing facility.

A simulation was set up to increase the system Reynolds number, $Re_c = \frac{\rho V_0 c}{\mu}$, by a factor of five, increasing it from $Re_c = 28,000$ to $Re_c = 140,000$. This was achieved in the simulation by decreasing the viscosity from $\mu = 1.002 \times 10^{-3} \frac{kg}{m-s}$ (characteristic of water) to $\mu = 0.2004 \times 10^{-3} \frac{kg}{m-s}$ while keeping all other parameters the same. This allowed all dimensions in the mesh, as well as the free stream velocity and rotational velocity to remain the same.

An additional needed change for simulating the higher Reynolds number, is the mesh refinement at the blade wall. In near-wall modeling, best results require $y^+ = \frac{\mu_\tau y}{\nu} \sim 1$.

By increasing the Reynolds number, the nearest node distance to the wall, y, must be decreased to meet the y^+ requirement. This means that a more refined mesh must be used. y^+ is a solution dependent parameter, so the finest mesh created for the mesh convergence study is used in an initial attempt to meet the y^+ requirement for the high-Reynolds number simulation. The results showed this mesh meets $y^+ \sim 1$ for most cells at the wall, and nearly all meet $y^+ < 5$. It is possible that a further refinement in the mesh may provide more accurate results.

While $Re_c = 140,000$ is higher than the original simulation, both are still in the low-to-moderate range of Reynolds numbers for turbulent flow. At these lower Reynolds numbers, the coefficients of lift and drag for an airfoil or hydrofoil vary significantly, as shown previously by the Sandia National Laboratories data in figure 5.9. As the Reynolds number increases, the ratio of lift to drag increases as well, indicating an improvement in turbine performance at the higher Reynolds numbers. Figure 5.11 shows the plots of the hydrodynamic torque for the original Reynolds number and for the case of the higher Reynolds number for $\lambda = 3.2$. As expected, an increase in the instantaneous torque and average torque of the cycle for the $Re_c = 140,000$ is evident. This corresponds to an increase from 21% to 42% in turbine power efficiency.

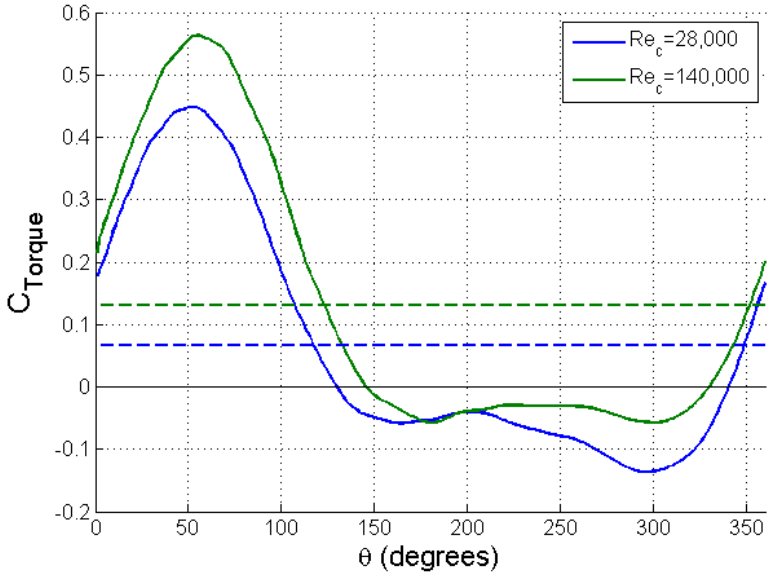

Figure 5.11: Instantaneous and average torque for for a single blade rotating at $\lambda = 3.2$ at an increased Reynolds number

5.2 Four-Bladed Rotating Turbine

5.2.1 Numerical Simulations

Numerical simulations for a four-bladed rotating turbine were performed for three tip speed ratios: $\lambda = 1.3$, $\lambda = 1.6$, and $\lambda = 2.0$. Figure 5.12 shows the case for $\lambda = 1.6$. The instantaneous hydrodynamic torque for each of the blades as well as the instantaneous total turbine torque are shown. The average torque for the turbine of the cycle is also provided. As expected, the total turbine torque stays approximately constant through the rotation and each blade has an almost identical hydrodynamic torque curve, with offsets of 90°. The cases for $\lambda = 1.3$ and $\lambda = 2.0$ have qualitatively similar results.

The effect of increasing the turbine solidity ratio can be isolated by comparing the simulation results for the single-bladed turbine to an individual blade of the four-

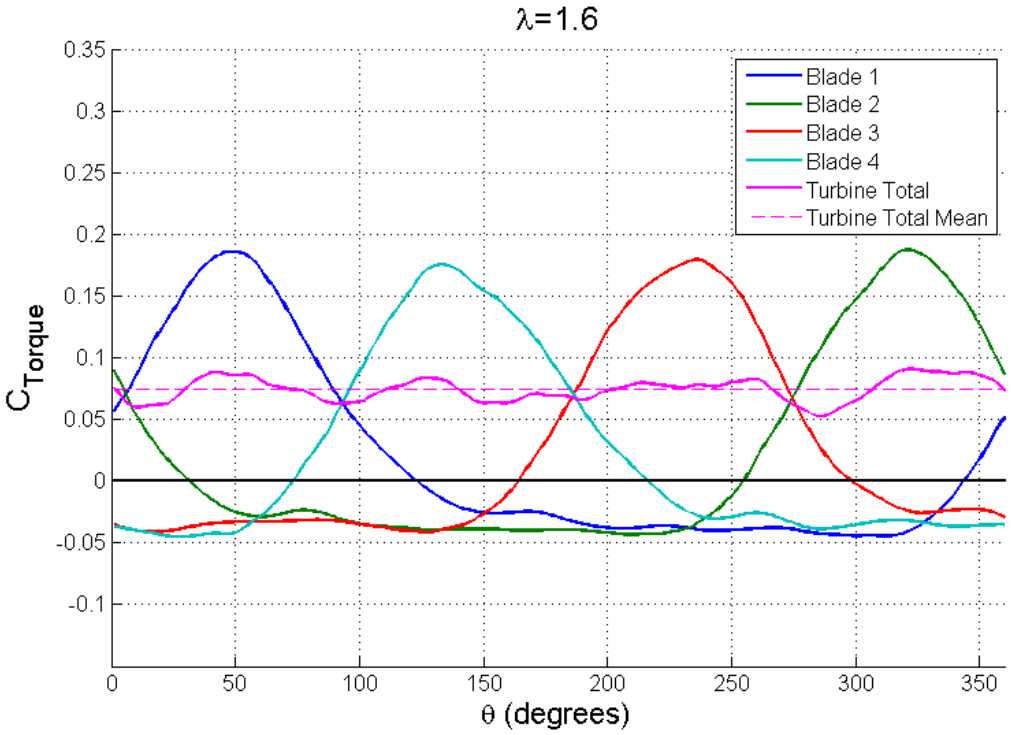

Figure 5.12: Instantaneous and average torque for four-bladed rotating at $\lambda = 1.6$

bladed turbine at $\lambda = 1.6$ as shown in figure 5.13. We increase the solidity by a factor of four, from $\sigma = 0.075$ for a single blade to $\sigma = 0.30$ for four blades. At $\lambda = 1.6$, the increase in solidity creates higher impedance to the flow, leading to a lower torque for an individual blade, but the total torque for the four-bladed turbine is still greater than the total turbine torque for a single-bladed turbine. At a high enough tip speed ratio (or rotational velocity at a constant free stream flow velocity), high solidity creates a large enough impedance that the torque for a single blade is actually larger than for the full four-bladed turbine. This can be observed in 5.14 which shows the torque predictions from the CFD simulations. At tip speed ratios higher than the intersection point of the two torque curves, the single blade turbine has a higher predicted hydrodynamic torque. The effect of solidity on turbine performance is also

confirmed by the experimental results: higher rotational velocities could be reached by the single-bladed turbine compared to the four-bladed configuration, showing that it could overcome higher frictional torque. The right balance between solidity and tip speed ratios provides the turbine's optimum dynamic performance. Our results show evidence in a three dimensional simulation and experiments of the influence of solidity ratio on turbine performance. Consul et al. [29] predicted similar results in two-dimensional simulations for rotating two- and four-bladed Darrieus cross-flow turbines.

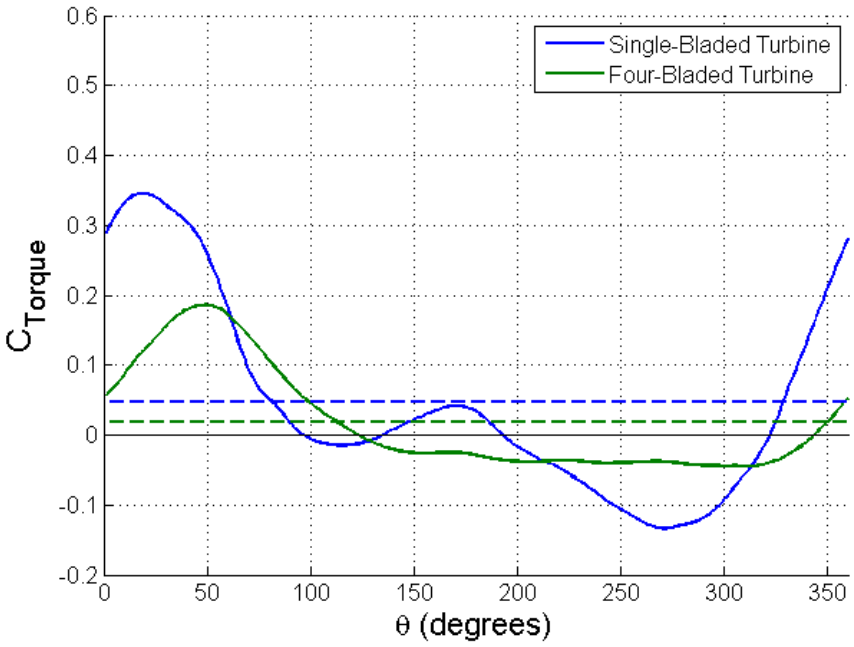

Figure 5.13: Instantaneous torque for a single-bladed turbine and four-bladed turbine rotating at $\lambda = 1.6$

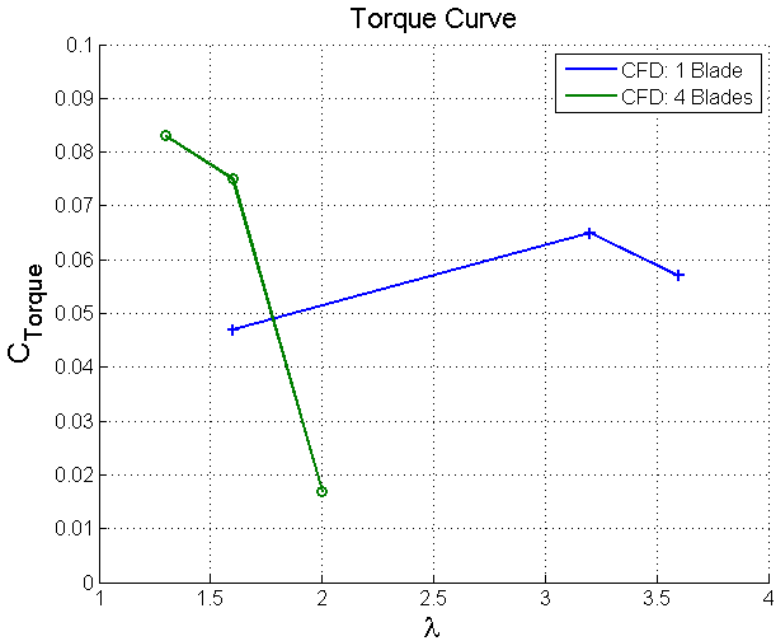

Figure 5.14: Plot of CFD predicted torque values vs. tip speed ratio

5.2.2 Comparison of the Simulation results with the Experiments

Figure 5.15 shows a plot of the torque and power curves from the experiments as well as the data from the simulations. There is very good qualitative agreement; however, the simulation predicts lower performance for all three tip speed ratios. We hypothesize that this discrepancy is due to the effect of dynamic stall that delays separation, increasing the range of angles of attack where the blades are producing significant hydrodynamic lift and torque. This phenomenon is present in the experiments but may not be well captured by the simulation.

A rotating blade has different stall characteristics than a static airfoil or hydrofoil. In a Cross Flow Turbine hydrofoil, the angle of attack is changing rapidly, which can delay the angle at which stall occurs to an extent that far exceeds the static stall angle [38]. It has already been shown from the static turbine case, that the Reynolds Averaged Navier Stokes equations have difficulty predicting separation in the stall region. The

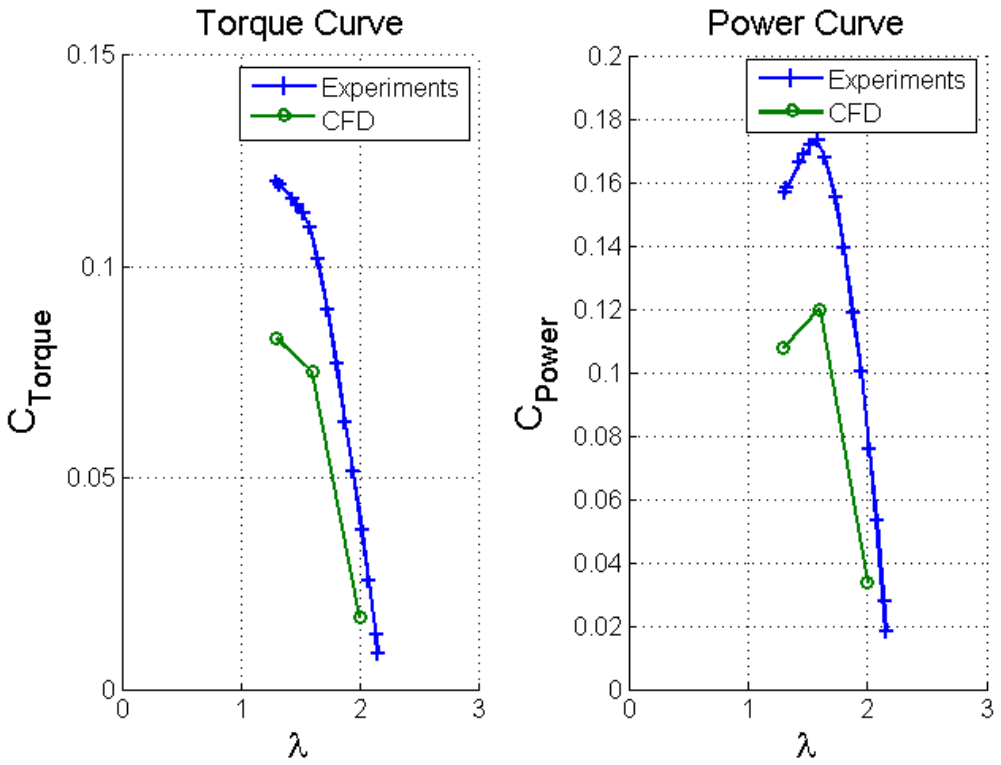

Figure 5.15: Torque and power curves for a four bladed turbine: experiments and simulations

simulation is not expected to be able to capture the dynamic stall phenomenon and, therefore, predicts separation prior to when it occurs in the experiment, leading to a lower predicted torque.The over-prediction of performance for the static turbine is consistent with the attribution of the under-prediction of performance in the rotating case to dynamic stall. In the static turbine there is no dynamic stall and the RANS equations tend to predict separation at higher angles of attack than experimentally observed, leading to the over-prediction for the static case.

In the dynamic turbine case, the difference in predicted versus measured performance is largest for simulations at lower tip speed ratios. Operating at lower tip speed ratio, the turbine blades reach higher angles of attack and have lower relative Reynolds

numbers. These two parameters make the flow more prone to separation and are consistent with the under-prediction of torque and power by the CFD, where there is no dynamic stall to delay separation, compared to the experiments.

The torque predictions from single-blade and four-blade turbine simulations differ in an important aspect: for the single blade case ($\lambda = 3.2$ and $\lambda = 3.6$), the simulations over-predict the torque compared to experiments, while in the four-blade case ($\lambda = 1.3$, $\lambda = 1.6$, and $\lambda = 2.0$), the simulations under-predict the torque. Our hypothesis is that dynamic stall is present in both the four-bladed turbine as well as the single blade. The lack of accurate dynamic stall prediction in the RANS simulations leads to over-predicting torque in the four-bladed turbine but is overwhelmed by other sources of error in the single blade simulations. These other errors have the opposite effect as dynamic stall and therefore tend to under-predict torque. The key source of error in the single blade simulations is the modeling at constant rotational speed (near the value for peak torque) while the experiments take place at oscillating rotational speeds. Additionally, the higher rotational speeds for the single-bladed turbine suggest that the frictional torque component of the system is larger for the single blade cases. This higher frictional torque component favors the simulation over-predicting the experimental torque measurements. Lastly, at the higher tip speed ratios fo ther single blade turbine, the angle of attack is lower and the Reynolds number higher, so the effect of dynamic stall will be minor and therefore its influence on torque predictions will be negligible or minor.

The mesh convergence test was performed for a high rotational velocity. The results suggest that the lower tip speed ratio simulations could possibly see improved results with a more refined mesh because of difference in stall dynamics between the simulation and experiment growing at lower rotational speeds; however, a finer mesh may still have difficulty capturing the dynamic stall phenomenon. Despite the lower values of torque and power predicted from the simulations, there are very good qualitative results, suggesting this methodology can be used to study turbine design and per-

formance over a wide range of parameters. Further experimentation can be reduced by proceeding only with the CFD cases that predict optimum turbine design options and specially relevant operating parameters, efficiently using experimental resources.

Chapter 6

SUMMARY, CONCLUSIONS AND FUTURE WORK

Tidal flows have been realized as a potential renewable resource for energy harvesting and electricity generation. Though energy conversion from tidal flows shares many similarities to wind energy, the application of turbine technology to Marine Hydrokinetic (MHK) Turbines creates new challenges and involves different physical considerations. In recent decades, the wind industry zeroed in on the Horizontal Axis Wind Turbine (HAWT) as the best choice for utility-scale electricity generation, based on efficiency and scalability, and developed and optimized this technology. The understanding of cross flow turbines has remained far behind as a result. In recent years, there has been renewed interested in developing the Cross Flow Hydrokinetic Turbine (CFHT) technology due to its potential advantages in the marine hydrokinetic application, where the differences with wind in scale, installation cost and reversible currents can make CFHTs a viable alternative to Horizontal Axis Hydrokinetic Turbines. This thesis has developed a methodology for numerical modeling of helical-bladed cross flow hydrokinetic turbines. This design is similar to a Gorlov turbine. The numerical model has been validated against experimental results. The strengths and challenges of the methodology have been identified and a better understanding of the complex physics of a CFHT has been achieved. The ultimate goal is to provide a computational tool that can support the turbine design and array installation process with detailed hydrodynamic data, at relatively short turn around and low cost. This will minimize the number of prototypes built and experiments run, limiting them to the selected few identified as optimum or near-optimum by the computations. The powerful combination of detailed simulations and targeted experiments will speed up

the development of CFHT technology and bring it to fruition in the form of projects installed and cost-effective environmentally-friendly electricity generated from this renewable source.

6.1 Numerical Methodology

The Reynolds Average Navier Stokes (RANS) equations with a SST-kω turbulence closure model were applied using the commercial computational fluid dynamics software ANSYS FLUENT v12.0. A highly detailed computational mesh around the geometry of the turbine blades and a transient solver were employed to achieve a time-accurate solution for the highly unsteady and three-dimensional flow of a CFHT. To simulate the rotating turbine, the sliding mesh technique was used. The three-dimensional sliding mesh technique is more computationally intensive than most other methodologies in current literature for CFHT, but is necessary to accurately predict the instantaneous features of flow around a helical-bladed turbine.

6.2 Analysis of the Static Turbine Performance: Starting Torque

Simulations were performed for a single blade and a four-bladed configuration of a static turbine and the results from the model were compared with experimental measurements under the same conditions. The static torque analysis provides insight into the start-up characteristics of the turbine.

The simulation results for flow over a single-static blade showed very good agreement with the experiment for most azimuthal locations, both in their qualitative trends and in the quantitative value predictions. The positions where the quantitative agreement was not achieved were located between 315° and 45°, in the region where the blade operates at moderate angles of attack. This result highlights the RANS equations' inherent inability to accurately predict the location of separation of flow in the boundary layer due to a smooth negative pressure gradient which is present during static stall (approximately $|\alpha| > 15°$). Flow was accurately simulated at angles of attack

below static stall, but a blade with sections in this region also has large sections in the stall region, leading to an over-prediction of torque for that blade position. At very large angles of attack, where the flow is coming almost perpendicular to the blade, or when the flow is coming at the blade from the trailing edge, sudden negative pressure gradients are imposed by the blunt geometry, and the location of separation is predicted accurately. The different near-wall modeling options were investigated. Refining the grid near the blade wall to resolve the viscous sublayer resulted in a reduction in error at positions when static stall was present, but came with much greater computational costs.

Simulations for a four-bladed static turbine compared to experiments showed similar discrepancies as in the single blade case due to the same modeling difficulties for smooth negative pressure gradients, but the results gave a good general static torque prediction. The static torque is approximately the same for all azimuthal positions, as expected in this turbine design where the four blades wrap homogeneously around the circumference. The experiments show a very large drop in torque for $\theta = 70°$, due to a wake created by the blades on the upstream side of the turbine affecting the turbine blades directly downstream. The simulation does not capture this wake-blade interaction, likely due to numerical error that diffuses the wake more quickly than in the experiment.

Comparing the simulations for a single-blade turbine and a four-blade turbine on an individual blade basis does show some significant changes in the torque, due to wake-blade interactions present in the four-blade case. In line with the experiments, there is a general trend of a small increase in predicted torque per blade for the four-bladed turbine simulation compared to the single blade simulation. We hypothesize that this increase in static torque performance is due to the increase in solidity and blockage ratio associated with the four-bladed turbine configuration.

6.3 Summary of Dynamic Turbine Analysis

Simulations were performed for a rotating turbine operating at different tip speed ratios. Both a single-blade and four-blade configuration of the rotating turbine was investigated. A mesh convergence study was performed, and experiments were used to validate the simulation results. The effects of increasing the Reynolds number and also of increasing the number of blades, therefore increasing the solidity, were explored computationally.

6.3.1 Single-Bladed Rotating Turbine

The independence of the simulation results with refinement of the numerical discretization was confirmed for a specific simulation: single blade operating at $\lambda = 3.2$. Three grids of varying levels of refinement were tested. For a static turbine, modeling in the near-wall region using the wall function approach was adequate for most blade orientations; however because a rotating turbine sees rapidly changing angles of attack, it was evident that a finer mesh which used the near-wall modeling approach was required for the dynamic model. We found an adequate compromise between convergence and computational cost in a mesh with about 5 million grid points and wall spacing $y^+ \approx 2$.

Three tip speed ratios, $\lambda = 1.6,\ 3.2$, and 3.6, were simulated for a single blade, and the hydrodynamic torque as a function of the blade's azimuthal position was analyzed. Each operating speed has peak torque values at approximately $\theta = 45°$ and $\theta = 235°$, which corresponds to the turbine being centered around $\theta = 90°$ and $\theta = 270°$. This agrees very well with theory: the peaks for the turbine curves should occur when the angle of attack reaches its maximum pre-stall angle of about 15°, which happens around $\theta = 90°$ and $\theta = 270°$ for the tip speed ratios of 3.2 and 3.6, and earlier, around $\theta = 50°$ for the tip speed ratio of 1.6. The peak for the blade's position of $\theta = 235°$ is much lower due to the velocity deficit and wake effects from the upstream

side of the turbine rotation.

The model was validated against experiments performed for a single blade rotating at $\lambda_{avg} = 3.2$ and $\lambda_{avg} = 3.6$. The large oscillations of hydrodynamic torque acting on the very low-inertia blade created a significant variation in the angular velocity over each turbine cycle in the experiment. These accelerations in angular velocity create a large disparity between what the reaction torque cell measures and the hydrodynamic torque of the experiment, meaning a direct comparison between the numerically simulated hydrodynamic torque and experimental raw torque data cannot be made. An additional and very important step is taken to calculate the angular acceleration of the blade as a function of azimuthal position, from the experimental data collected. The inertial term in the angular momentum equation for the system is then calculated and added to the torque sensor measurements, creating a more appropriate dataset for comparison with the turbine's hydrodynamic torque CFD prediction.

For both values of the tip speed ratio, we found an over-prediction of the average torque by the CFD model, but also observed very similar qualitative and quantitative features in the instantaneous torque curves. Differences in the two datasets are attributed to the simulation modeling the system at a constant tip speed ratio while the experiments actually have significant variations in angular velocity within each cycle. The varying rotational velocities, in addition to the frictional torque present in the system but not represented in the numerical model, account for the over-prediction in average torque.

The frictional torque of the system is hypothesized to increase with increasing rotational velocity. An effort was made to better characterize the frictional torque as a function of the rotational velocity by calculating the difference between the CFD and experimental torque curves; however this difference showed no consistent dependency on the rotational speed. The difference between the experimental and computational torque values is likely dominated by the disparity between the hydrodynamics at constant tip speed ratio in the numerical model and that at large variations in tip speed

ratio in the experiments. Thus, the characterization of the friction torque using this method is difficult and yields uncertain results.

While a direct comparison between the CFD and experiment proved challenging, the similarities in the torque curves for the experiments and model indicate the sliding mesh technique applied with the RANS equations can simulate the hydrodynamic torque of a CFWT with an acceptable level of accuracy.

A benefit of numerical simulation is the ability to change and study several parameters with greater ease and flexibility than for an experimental setup. The CFD simulations were computed to match the laboratory set-up which operates at a much lower Reynolds number than that of either a commercial scale turbine or the full-scale micropower turbine. In the interest of predicting the turbine's performance at a larger scale, a simulation for a higher Reynolds number was performed. The Reynolds number was increased by a factor of five by decreasing the viscosity of the fluid. Additionally, a more refined mesh was used to meet near-wall modeling requirements. The high Reynolds number simulation predicted a significant improvement in the turbine performance. This finding agrees well with tabulated airfoil coefficient data that show, for this low-Reynolds number regime, considerably more favorable ratios of lift to drag coefficients for a higher Reynolds number.

6.3.2 Four-Bladed Rotating Turbine

Numerical simulations for a four-bladed turbine were run for tip speed ratios of $\lambda =$ 1.3, 1.6, and 2.0. Due to the blades being evenly distributed around the full 360 circumferential degrees, the total turbine torque stays approximately constant through the rotation, while the individual blades have almost identical hydrodynamic torque curves with offsets of 90°.

The effect of increasing the turbine solidity ratio is investigated by comparing the torque of a single-blade turbine and a four-blade turbine operating at $\lambda = 1.6$. By increasing the number of blades, we increase the solidity ratio by a factor of four,

which creates a larger impedance to the flow. At $\lambda = 1.6$, this increase leads to an individual blade in the four blade configuration to have a lower average torque than the single blade case, though the total torque for the four blade configuration is still higher. It is evident from both the simulations and the experiments that at very high tip speed ratios, the impedance becomes so large for the high solidity turbine, the torque for the single blade turbine is actually higher than the total torque for the four blade turbine. These results emphasize that the right balance between solidity ratio and tip speed ratio must be found for optimum turbine performance.

When the simulations for the four-bladed case are compared against the experiments, we find very good qualitative agreement. The simulations do, however, show an under-prediction in the torque compared to the experiments. We hypothesize that this discrepancy is caused by the dynamic stall phenomenon that is present in the experiments but may not be well captured by the simulation. At lower tip speed ratios, the turbine blades reach higher angles of attack and have lower relative Reynolds numbers making the flow more prone to separation. Because the numerical model does not accurately simulate dynamic stall which delays the separation, there is an under-prediction of torque compared with the experiment. Despite this disparity, the very good qualitative agreement suggests promising results for using the methodology to predict optimum turbine design and operating parameters.

6.4 Conclusions and Future Work

In this thesis a numerical methodology was developed to model a helical-bladed CFHT. Analysis of static cases, as well as turbine operations in steady-state rotation at different tip-speed ratios, was conducted from the simulations results. We concluded that the methodology we have developed can accurately model the starting torque of a turbine, under static conditions, with some limitations associated with predictions of separated flow in RANS simulations. The sliding mesh model for the rotating turbine provided excellent qualitative results and good quantitative agree-

ment with the experimentally measured values, but showed issues with accurately modeling dynamic stall phenomenon that translated in small deviations in the actual values predicted for performance.

Development of numerical tools to predict turbine performance and environmental effects are an essential engineering step to developing MHK turbine technology in a cost-effective and time-efficient manner. Blade design, turbine support structure, and array optimization can be achieved using a numerical model without the need for multiple expensive and time consuming manufacturing and testing operations. Full-scale turbine performance can also be estimated prior to deployment. Additionally, environmental effects can be predicted "in-silico", without any risk from testing and experimentation. While numerical models have many advantages, it is also important to understand their limitations. It is our hope that this model and its future developments can be used to better understand the flow physics, performance, and potential environmental impacts of a cross flow hydrokinetic turbine, and aid in the implementation process of MHK turbine technology as an economically viable, environmentally-friendly source of electricity on a commercial scale.

BIBLIOGRAPHY

[1] European Commission. *Climate Action*, 2010. URL http://ec.europa.eu/clima/policies/package/index_en.htm.

[2] U.S. Department of Energy. *Energy Efficiency & Renewable Energy*, 2009. URL http://apps1.eere.energy.gov/states/maps/renewable_portfolio_states.cfm#chart.

[3] Institute for Energy Research. *Washington Renewable Electricity Mandate Standard*, 2011. URL http://www.instituteforenergyresearch.org/wp-content/uploads/2010/12/Washington-RPS.pdf.

[4] U.S. Department of Energy. *Database of State Incentives for Renewables & Efficiency*, 2011. URL http://www.dsireusa.org/incentives/incentive.cfm?Incentive_Code=WA15R&re=1&ee=1.

[5] J. Twidell and T. Weir. *Renewable Energy Resources, Chapter 13*. Taylor & Francis, 2006.

[6] Windows to the Universe. 2009. URL http://www.windows2universe.org/earth/Water/ocean_tides.html.

[7] P. Fraenkel. Tidal turbines harness the power of the sea. *Reinforced Plastics*, 48 (6):44 – 47, 2004.

[8] S. Antheaume, T. Maitre, and J. Achard. Hydraulic darrieus turbines efficiency for free fluid flow conditions versus power farms conditions. *Renewable Energy*, 33(10):2186 – 2198, 2008.

[9] Federal Energy Regulatory Commission. *FERC Issues First Pilot License for Tidal Power Project in New York*, 2010. URL http://www.ferc.gov/media/news-releases/2012/2012-1/01-23-12.asp.

[10] J. Zanette, D. Imbault, and A. Tourabi. A design methodology for cross flow water turbines. *Renewable Energy*, 35(5):997 – 1009, 2010.

[11] A.S. Bahaj and L.E. Myers. Fundamentals applicable to the utilisation of marine current turbines for energy production. *Renewable Energy*, 28(14):2205 – 2211, 2003.

[12] W.M.J. Batten, A.S. Bahaj, A.F. Molland, and J.R. Chaplin. Hydrodynamics of marine current turbines. *Renewable Energy*, 31(2):249–256, Feb 2006.

[13] P. Fraenkel. Windmills below the sea: A commercial reality soon? *Refocus*, 5 (2):46 – 50, 2004.

[14] M. Kawase, P. Beba, and B.C. Fabian. Finding an optimal placement depth for a tidal in-stream energy conversion device in an energetic, baroclinic tidal channel. Technical report, University of Washington, 2011.

[15] M. Shiono, K. Suzuki, and S. Kiho. Output characteristics of darrieus water turbine with helical blades for tidal current generations. *Proceedings of the International Offshore and Polar Engineering Conference*, 12:859 – 864, 2002.

[16] A. Niblick. Experimental and analytical study of helical cross-flow turbines for a tidal micropower generation system. Master's thesis, University of Washington, 2012.

[17] M. Islam, D.S.K. Ting, and A Fartaj. Aerodynamic models for Darrieus-type straight-bladed vertical axis wind turbines. *Renewable & Sustainable Energy Reviews*, 12(4):1087–1109, MAY 2008.

[18] R.J. Templin. Aerodynamic performance theory for the nrc vertical-axis wind turbine. In *NRC Lab. report LTR-LA-190*, page 29, June 1974.

[19] J.H. Strickland. A performance prediction model for the darrieus turbine. In *International sumposium on wind enery systems, Cambridge, UK*, volume C3-39-54, 1976.

[20] I. Paraschivoiu. Double-multiple streamtube model for darrieus wind turbines. In *Second DOE/NASA wind turbines dynamics workshop, NASA*, volume 7, pages 416–421, 1983.

[21] H.C. Larsen. Summary of a vortex theory for the cyclogiro. In *Proc of the second US national conference on wind engineering research, Colorado State University*, volume 8, pages 1–3, 1975.

[22] J.H. Strickland, B. Webster, and T. Nguyen. A vortex model of the darrieus turbine: an analytical and experimental study. *Journal of Fluids Engineering*, 101:500–505, 1979.

[23] H. Hirsh and A.C. Mandal. A cascade theory for the aerodynamic performance of darrieus wind turbines. *Wind Engineering*, 11(3):164–175, 1987.

[24] L. Zori and R. Rajagopalan. Navier-stokes calculations of rotor-airframe interaction in forward flight. *Journal of the American Helicopter Society*, 40(2):57, 1995.

[25] S. Antheaume. Modeling a wind turbine comparisons of the srf and vbm models.

[26] T. Javaherchi. Numerical modeling of tidal turbines: Methodolgy development and potential physical environmental effects. Master's thesis, University of Washington, 2010.

[27] R.E. Sheldhal and P.C. Klimas. Aerodynamic characteristics of seven symmetrical airfoil sections through 180-degree angle of attack for use in aerodynamic analysis of vertical axis wind turbines. sand 80-2114. Technical report, SANDIA Laboratories, March 1981.

[28] T. Matre, J.L. Achard, L. Guittet, and C. Ploesteanu. Marine turbine development: numerical and experimental investigations. *Scientific Bulletine of the Politehnica University of Timisoara*, 50(64):59–66, 2005.

[29] C.A. Consul, R.H.J. Wilden, E. Ferrer, and M.D. McCulloch. Influence of solidy on the performance of a cross-flow turbine. In *Proc 8th European Wave and Tidal Energy Conference, Upsalla, Sweeden*, 2009.

[30] S. Lain and C. Osorio. Simulation and evaluation of a straight-bladed Darrieus-type cross flow marine turbine. *Journal of Scientific & Industrial Research*, 69 (12):906–912, 2010.

[31] S. Li and Y. Li. Numerical study on the performance effect of solidity on the straight-bladed vertical axis wind turbine. *2010 Asia-Pacific Power and Energy Engineering Conference, APPEEC 2010 - Proceedings*, pages IEEE Power and Energy Society (PES); State Grid of China; Siemens Ltd.; Sichuan University; Chongqing University –, 2010.

[32] Y. Sun and L. Zhang. Airfoil optimization of vertical-axis turbines based on cfd method. *ICCMS 2010 - 2010 International Conference on Computer Modeling and Simulation*, 3:199 – 202, 2010.

[33] M.R. Castelli and E. Benini. Effect of Blade Inclination Angle on a Darrieus Wind Turbine. *Journal of Turbomachinery-Transactions of the ASME*, 134(3), 2012.

[34] S.B. Pope. *Turbulent Flows, Chapter 10.* Cambridge University Press, 2008.

[35] W.P. Jones and B.E. Launder. The prediction of laminarization with a two-equation model of turbulence. *Int. J. Heat Mass Transfer*, 15:301–314, 1972.

[36] D.C. Wilcox. Turbulence modeling for cfd. *La Canada, CA: DCW Industries*.

[37] F. Menter. Two-equation eddy-viscosity turbulence models for engineering applications. *AIAA J.*, 32:1598–1605, 1994.

[38] John A. Ekaterinaris and Max F. Platzer. Computational prediction of airfoil dynamic stall. *Progress in Aerospace Sciences*, 33(11-12):759 – 846, 1997.

[39] *ANSYS FLUENT 12.0 theory guide, Chapter 4, Section 4.12, Near-Wall Treatments for Wall-Bounded Turbulent Flows*, 2011. URL https://www.sharcnet.ca/Software/Fluent12/html/th/node1.htm.

[40] *ANSYS FLUENT 12.0 user guide, Chapter 11, Section 11.2, Using Sliding Meshes*, 2011. URL https://www.sharcnet.ca/Software/Fluent12/html/ug/node389.htm.

[41] W.A. Basha and W.S. Ghaly. Drag prediction in transitional flow over airfoils. *Journal of Aircraft*, 44(3):824 – 832, 2007.

[42] P. Catalano and R. Tognaccini. Turbulence modeling for low-reynolds-number flows. *AIAA Journal*, 48(8):1673 – 1685, 2010.

[43] P. Catalano and R. Tognaccini. Rans analysis of the low-reynolds number flow around the sd7003 airfoil. *Aerospace Science and Technology*, 15(8):615 – 626, 2011.

[44] R.E. Sheldahl and P.C. Klimas. Aerodynamic characteristics of sevel symmetrical airfoil sections through 180-degree angle of attack for use in aerodynamic analysis of vertical axis wind turbines. Technical report, Sandia National Laboratory, 1981.